University of Iceland
Faculty of Natural Sciences
Department of Physics

RH-07-2007

Transport of an electron wave packet through a nanostructure in a magnetic field

by

Gunnar Þorgilsson

A thesis submitted in partial satisfaction
of the requirements for the degree of Master of
Science in Physics at the University of Iceland

Committee in charge:
Viðar Guðmundsson, Chair
Snorri Ingvarsson

Reykjavík
June 2007

Abstract

A model is developed for a time dependent transport of a wave packet through a quantum wire with an embedded nanostructure in a perpendicular homogeneous magnetic field. The model is built on the Lippmann-Schwinger formalism of scattering theory in coordinate-momentum space as introduced by Gurvitz [1]. Four different nanostructures are studied by using the model: a constriction, a quantum ring, a donor-like impurity and an acceptor-like impurity. In the results from the simulations we observe phenomena such as skipping orbits, self-interference, and mode mixing, effects which have all been seen in the static case [1–5]. In addition we observe time lags and transition to short or long lived intermediate states, effects that are not directly observable in the static case.

Acknowledgment

The work and research which is the subject of this thesis was carried out at the University of Iceland and was conducted under the supervision of Prof. Viðar Guðmundsson. His insight and interested in the field along with his optimism has proven invaluable to my research. I also deeply appreciate his patience and readyness to answer any question laid upon him. I would like to thank my family for their support throughout my studies at the University of Iceland and last but not the least I thank Berglind for her love and support.
This research was partly funded by the Research Fund of the Icelandic Science Council, the University of Iceland Research Fund, and the Science and Technology Research Programme for Postgenomic Biomedicine Nanoscience and Nanotechnology.

Contents

Chapter 1

Introduction

In recent years the ability to construct structures on smaller and smaller scale has improved dramatically. Systems where quantum properties of the electrons are clearly detectable have become more common through more elaborate fabrication techniques of semiconductors and the accessibility of ^{3}He -^{4}He refrigerator equipment, which can produce experimental temperatures in the 10 mK and 1 K range. This has introduced to us the regime of ballistic mesoscopic physics where elastic scattering length and phase coherence length of the electron are longer than the dimensions of the sample. Elaborate nanostructures can be constructed with lithographic methods and manipulated with equipments such as atomic force microscopes and electron tunneling microscopes. Some or all dimensions of a sample can be shortened down to Fermi wavelength of the electrons. This introduces interesting structures such as two dimensional electron gas (2DEG) structures, quantum wires and quantum dots where one, two or three dimensions of the structures have been reduced to a comparable length to the Fermi wavelength or shorter.

The focus of this thesis will be on calculations regarding transport of single electron or a burst of electrons in quasi one dimensional electron gas (q-1DEG) structures such as quantum wires with some nanostructure embedded in them. This has been done for the static case [1–5], where the wave function and conductance of a constant stream of plane wave like electrons has been calculated in q-1DEG structures. But by introducing time to these calculations we will strengthen our understanding of how electrons are transported through these systems and answer questions such as of the role of self-interference, mode mixing and skipping orbits in the transport of the electrons. Many different paths of modeling methods have been taken to get a time dependent picture of the flow of electrons in q-1DEG structures. These include adiabatic approximation [6], 1D approximation [7], density functional theory [8] and non-equilibrium Greens functions [9] to mention a few. But the path taken in this thesis will be via scattering theory in momentum-coordinate space, a method suggested by Gurvitz [1]. The aim is to produce a model that is capable of producing a time dependent picture of the evolution of a wave packet traveling through various q-1DEG structures.

This thesis is divided into 5 chapters along with this introduction chapter. In chapter 2 we will briefly look at how q-1DEG structures are constructed. The chapter ends with an attempt to consider in a practical way how to inject a single electron or a burst of electrons into the nanostructures and indirectly measure the evolution of the electron wave packet. Chapter 3 contains the detailed overview of the theory behind the simulations. In the former part of the chapter an equation for the evolution of the wave function in the leads will be developed along with discussion of the conductance in them. The latter part introduces a nanostructure to the leads and handles the derivation of the scattered wave function along with an equation for the static conductance through the nanostructure. Chapter 3 is accompanied by three appendixes at the end of the thesis. In chapter 4 the setup of the simulations will be described and results presented. Summary follows in chapter 5.

Chapter 2

Fabrication of quantum wires and experimental setup

This chapter will briefly introduce ways to construct a quantum wire containing some arbitrary potential geometry. To make such a system the height and width of it have to be of comparable size or smaller than the Fermi wavelength of the electrons which will be traveling through it. This will quantize the energy of the electrons in the directions perpendicular to the wire. We will begin by looking at how we can produce a two dimensional electron gas (2DEG) with GaAs and AlGaAs. Then we will move onto ways to transform the 2DEG into a quasi one dimensional electron gas (q-1DEG) and discuss the transport properties of such a structure. The last section in this chapter discusses ways to inject and measure single electrons in q-1DEG structures.

2.1 2DEG structures

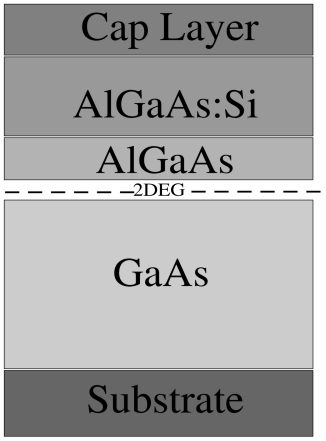

Figure 2.1: Schematic picture of the heterostructure.

A common way to make a 2DEG is to use a heterostructure made out of GaAs semiconductor and $Al_xGa_{1-x}As$ insulator (x is the concentration of Al in the compound). Because the GaAs crystal has a lattice constant of about 5.65 Å and the $Al_xGa_{1-x}As$ crystal a lattice constant of about 5.66 Å these two materials are very suitable to grow in layers with each other. A simple GaAs-$Al_xGa_{1-x}As$ heterostructure is made out of four different layers, see figure 2.1. These layers are grown in sequence atop of each other from a substrate, which is often a GaAs crystal. A layer of undoped AlGaAs is often included to reduce defect scattering caused by doping. On top of the heterostructure a cap of GaAs prevents the Al atoms to oxidize. To manufacture the heterostructure requires an accuracy of up to an atomic monolayer, if crystal defects are to be avoided. This kind of accuracy can be achieved with molecular beam epitaxy

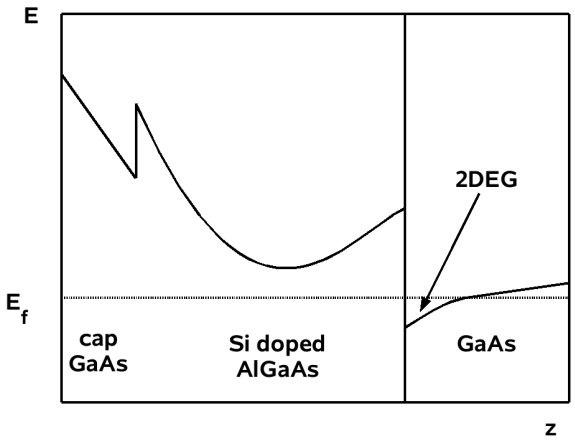

Figure 2.2: The conduction band in a GaAs-AlGaAs Heterostructure.

(MBE). GaAs-$Al_xGa_{1-x}As$ has a band gap of about (1.5 +0.7x) eV while GaAs has a smaller band gap of 1.5 eV. This causes electrons in the conduction bands to flow from the $Al_xGa_{1-x}As$ layers to the GaAs layer. But the structure is held at a low temperature which makes the GaAs semiconductor insulating. So the conduction bands of the GaAs in the first layer and the $Al_xGa_{1-x}As$ in the second layer are empty. Thus the only electrons capable of moving between the layers in this situation are electrons from the Si atoms which the third layer above the substrate is doped with. But the electrons which come from the Si atoms can not go very far because the Si atoms become positively charged and attract the electrons back towards them. This produces a profile of the conduction band which can be seen in figure 2.2. There we can see that a triangular energy well forms at the interface between the GaAs layer and the AlGaAs layer. In this well we can get an energy gap of roughly 20 meV between subbands. This energy gap is enough to "freeze" out the motion of the electrons in the z direction for temperatures lower than ≈ 100K which renders the system dynamically 2D [10, 11].

2.2 q-1DEG structures and their conductance properties

To further control the geometry of the system electrodes can be put on the cap layer. Putting negative voltage on these electrodes repels the electrons from the regions below them while positive voltage attracts them. A schematic arrangement of electrodes which produces a simple wire geometry containing some structure in the middle of it can be seen in figure 2.3. The new potential produced by the electrodes introduces new subbands in the electron gas. But because the electrons can jump between these new subbands the gas is a quasi one dimensional electron gas (q-1DEG) but not simply one

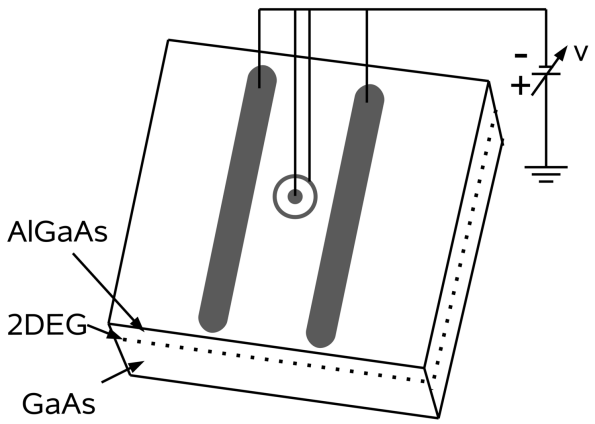

Figure 2.3: A schematic picture of how specific geometries can be formed with electrodes on heterostructures.

dimensional. The conductance of such a structure has experimentally been shown to be quantized with roughly a double conductance quantum, $2e^2/h$. Analytically this behavior can be described with the Landauer formula

$$G = G_0 \mathrm{Tr}[\mathbf{t}^\dagger \mathbf{t}] \tag{2.1}$$

where $G_0 = \frac{2e^2}{h}$ and $\mathbf{t}$ is the transmission matrix [10, 12].

2.3 Injecting and measuring a single electron in q-1DEG structures

The simulations which this thesis covers all assume a wave packet being injected into the q-1DEG structures. This could be done in the laboratory by using single electron tunneling. That process can be achieved by using a double barrier structure which serves as a quantum dot with discrete energy levels, also known as a single electron transistor (SET). By connecting an electrode to the structure the energy levels can be tuned to open or close a path for a single electron to tunnel through it [13, 14]. Measuring the evolution of the wave packet is a trickier business because it can not be measured directly. But there are indirect ways. One way is scan over the cap layer of the heterostructure with a tip of an atomic force microscope (AFM) which is biased with some potential V. The electric field of the tip alters locally the electrostatic potential below it which affects the conductance through the structure. How much it alters the conductance depends on how likely it was that the electrons traveled through the point below the AFM tip in the original electrostatic potential. This can then be used to roughly build up a picture of the wave function of the electrons [15, 16]. This

method has only been used for a continuous stream of electrons which corresponds to the results from the time independent calculations. To get measurements appropriate for time dependent calculations a scan of the time when the voltage of the AFM tip is activated could be performed. An another way to measure the wave function is to use the ability of GaAs to be double refracting which means that the crystal has different diffraction coefficient for different crystal direction. This quality of the crystal depends upon the electron density in the crystal [17]. So by irradiating the crystal with unpolarized light and measuring the change between the two differently refracted light beams from the crystal, one could measure the change of the electron density in the crystal. Which would enable us to construct a picture of how the wave packet evolves while traveling through the q-1DEG structures.

Chapter 3

Electronic transport in parabolic quantum wires connected to a nanostructure

In this chapter the theory used in the simulations will be explained. The first section handles derivation of the wave function in the leads and is followed by a section where we discuss the conductance through them. In the third section we will turn our attention to deriving the equation for the wave function of the electron scattering from the embedded nanostructure. The chapter ends with a derivation for the static conductance through the nanostructure. Calculations of matrix elements of the T-matrix and the matrix elements of the embedded potential along with the full analytical solution for the initial wave packet has been put in corresponding appendixes at the end of the thesis.

3.1 Wave function in a parabolic quantum wire

We will begin by deriving the wave function for a parabolicly shaped quantum wire in a homogenous magnetic field. It will be assumed that the wire lies along the x-axis of a 2 dimensional plane and is confined by a harmonic potential in the y direction of that plane. This corresponds to an one particle Hamiltonian of the form

$$H = \frac{p^2}{2m^*} + V_{\text{conf}} = \frac{p_x^2}{2m^*} + \frac{p_y^2}{2m^*} + \frac{1}{2}m^*\Omega_0^2 y^2. \tag{3.1}$$

Here m^* is the effective mass of electrons in GaAs, which we will assume the wire is made of, and Ω_0 is the strength of the confinement potential. As mentioned before we will also apply a homogenous magnetic field $\vec{B}$, which will be directed in the z direction perpendicular to the plane. This magnetic field can be described in the Landau gauge by a vector potential $\vec{A} = -By\hat{x}$ affecting the electron momentum

operator in the x direction in the following way

$$p_x = -i\hbar\frac{\partial}{\partial x} \quad \rightarrow \quad \pi_x = -i\hbar\frac{\partial}{\partial x} + \frac{e}{c}A_x. \tag{3.2}$$

Inserting this effective momentum operator in the x direction along with the usual momentum operator in the y direction, $p_y = -i\hbar\frac{\partial}{\partial y}$, into equation (3.1) we get the following real space representation of the Hamiltonian

$$\begin{aligned} H &= \frac{1}{2m^*}\left(-i\hbar\frac{\partial}{\partial x} + \frac{e}{c}A_x\right)^2 - \frac{1}{2m^*}\left(-i\hbar\frac{\partial}{\partial y}\right)^2 + \frac{1}{2}m^*\Omega_0 y^2 \\ &= -\frac{\hbar^2}{2m^*}\left(\frac{\partial^2}{\partial x^2} + \frac{\partial^2}{\partial y^2} - \frac{2i}{l^2}y\frac{\partial}{\partial x} - \frac{y^2}{l^4}\right) + \frac{1}{2}m^*\Omega_0^2 y^2, \end{aligned} \tag{3.3}$$

where $l^2 = \hbar c/Be$. With this Hamiltonian we can calculate the wave function from the Schrödinger equation

$$i\hbar\frac{\partial}{\partial t}\Psi(x,y,t) = H\Psi(x,y,t). \tag{3.4}$$

Because the wire is homogenous in the x direction we would expect to be able to separate the equations in momentum-coordinate space [1]. We therefore project the total wave function onto a base of plane waves traveling along the x-axis

$$\Psi(x,y,t) = \int\frac{dp}{\sqrt{2\pi}}\int\frac{d\omega}{\sqrt{2\pi}}e^{i(px-\omega t)}\Psi(p,y,\omega). \tag{3.5}$$

This will result in an equation for the Fourier components of the wave function

$$\hbar\omega\Psi(p,y,\omega) = \left\{-\frac{\hbar^2}{2m^*}\left(-p^2 + \frac{\partial^2}{\partial y^2} + \frac{2}{l^2}yp - \frac{y^2}{l^4}\right) + \frac{1}{2}m^*\Omega_0^2 y^2\right\}\Psi(p,y,\omega). \tag{3.6}$$

By doing some rewriting we will be able to transform equation (3.6) into

$$\left\{\frac{2m^*\omega}{\hbar} - p^2 + \frac{m^{*2}\Omega_w^2}{\hbar^2}\left(\frac{a_w^2\omega_c}{\Omega_w}p\right)^2 + \underbrace{\frac{\partial^2}{\partial y^2} - \frac{m^{*2}\Omega_w^2}{\hbar^2}\Big[y - y_0(p)\Big]^2}_{H_y}\right\}\Psi(p,y,\omega) = 0, \tag{3.7}$$

where $\omega_c^2 = \hbar^2/m^{*2}l^2$, $\Omega_w^2 = \Omega_0^2 + \omega_c^2$, $a_w^2 = \hbar/m^*\Omega_w$ and $y_0(p) = (a_w^2\omega_c/\Omega_w)p$. Here a_w is an effective magnetic length which takes the role of the radius of the classical circular motion of a particle in constant magnetic field. This will be used as a length scale in the numerical calculations. By examining equation (3.7) we see that the perpendicular part is a shifted harmonic oscillator Hamiltonian

$$H_y\Phi_n(y - y_0(p)) = \frac{2m^*E_n}{\hbar^2}\Phi_n(y - y_0(p)), \tag{3.8}$$

where $\Phi_n(y-y_0(p))$ are the eigenfunctions of the harmonic oscillator Hamiltonian and $E_n = \hbar\Omega_w\left(n+\frac{1}{2}\right)$ are the eigenvalues. The variables $y_0(p)$ and Ω_w have their origin in the Lorentz force. Effectively the Lorentz force offsets the parabolic potential by $y_0(p)$ on the y-axis for each plane wave component and changes the strength of the potential from Ω_0 to Ω_w. It is clear that the Fourier components of the wave function $\Psi(x,y,t)$ are best expanded over a base of shifted harmonic oscillator functions of the form $\Phi_n(y-y_0(p))$

$$\left\{\frac{2m^*\omega}{\hbar} - p^2 + \frac{m^{*2}\Omega_w^2}{\hbar^2}\left(\frac{a_w^2\omega_c}{\Omega_w}p\right)^2 + E_n\right\}\varphi_n^0(p,\omega)\Phi_n(y-y_0(p)) = 0. \tag{3.9}$$

Now by doing some rewriting again and taking the inner product with $\Phi^*_{n'}(y-y_0(p))$,

$$\int_{-\infty}^{\infty} dy\Phi^*_{n'}(y-y_0(p))\Phi_n(y-y_0(p)) = \delta_{n'n}, \tag{3.10}$$

an equation for a free particle traveling along the x-axis in subband n emerges

$$\left\{\hbar\omega - E_n - \frac{a_w^2\hbar}{2}\frac{\Omega_0^2}{\Omega_w}p^2\right\}\varphi_n^0(p,w) = 0. \tag{3.11}$$

An explicit momentum-energy relation can be read from equation (3.11) by multiplying $2\Omega_w/\hbar\Omega_0^2$ through the equation,

$$\left\{(k_n(\omega)a_w)^2 - (pa_w)^2\right\}\varphi_n^0(p,w) = 0, \tag{3.12}$$

or

$$k_n(\omega) = \pm\sqrt{\frac{2\Omega_w}{a_w^2\hbar\Omega_0^2}(\hbar\omega - E_n)}. \tag{3.13}$$

The solution to equation (3.11) is therefore a planewave type wave function traveling either way along the wire with an undetermined function $2\pi g_n(p)$ that represents the initial condition

$$\varphi_n^0(p,\omega) = 2\pi g_n(p)\delta\left[\omega - \left(\frac{E_n}{\hbar} + \frac{a_w^2}{2}\frac{\Omega_0^2}{\Omega_w}p^2\right)\right]. \tag{3.14}$$

By inserting (3.14) into (3.5) and remembering that we expandend $\Psi(p,y,\omega)$ in a bases of shifted harmonic oscillator wave functions, we get a general solution for the wave function traveling through the wire

$$\Psi(x,y,t) = \sum_n \int_{-\infty}^{\infty} dp g_n(p) e^{i\left(px - \left(\frac{a_w^2}{2}\frac{\Omega_0^2}{\Omega_w}p^2 + \frac{E_n}{\hbar}\right)t\right)}\Phi_n(y-y_0(p)). \tag{3.15}$$

To calculate the integral in equation (3.15) we will need to decide what to choose as an initial condition $g_n(p)$. In appendix C the integral is calculated for a Gaussian shaped wave function as an initial condition.

3.2 Conductance through a parabolic quantum wire

By examining the momentum-energy relation in (3.13) we can draw a picture of the subbands. In figure 3.1 the four lowest subbands have been plotted. There we see that for an electron to get into the lowest subband, and therefore into the wire, it has to have at least an energy of 0.5 $\hbar\Omega_w$. Each subsequent band above the lowest requires an extra $n\hbar\Omega_w$ energy quantum, where $n \in \mathbb{N}_+$. If we subtract in each band the energy quantum required to get into the band the momentum-energy relation has the same form as for a free particle. Now because only two electrons with forward momentum can occupy each subband at a given point in the wire, one with spin up and the other with spin down, the conductance comes in steps. The size of these steps are $G_0 = 2e^2/h$, were e^2/h is the conductance quantum. With this analysis we make a conductance plot for a parabolic quantum wire which can be seen in figure 3.2.

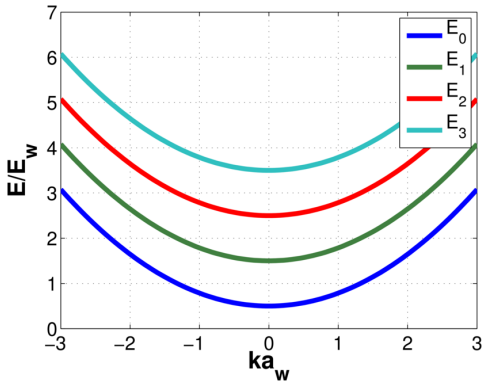

Figure 3.1: The four lowest subbands plotted for a parabolic quantum wire. The momentum is scaled in the inverse effective magnetic lengths a_w^{-1} and the energy in $E_w = \hbar\Omega_w$.

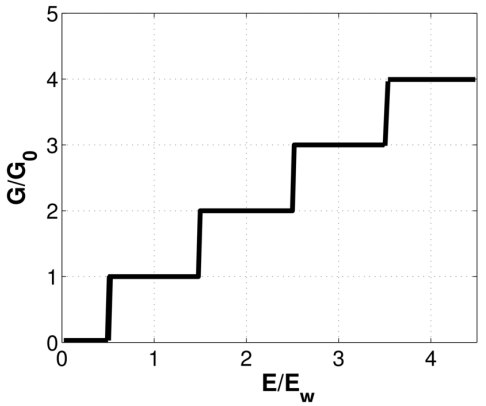

Figure 3.2: Conductance plot for a parabolic quantum wire. The energy is scaled in $E_w = \hbar\Omega_w$ and the conductance in the double conductance quantum $G_0 = 2e^2/h$.

3.3 Scattering in a nanostructure connected to quantum wires

We will use the model for the parabolic quantum wire which we developed in section 3.1 as leads that connect to a nanostructure. This configuration is divided into three regions; one scattering region containing the nanostructure and two leads, one on each side, see figure 3.3.

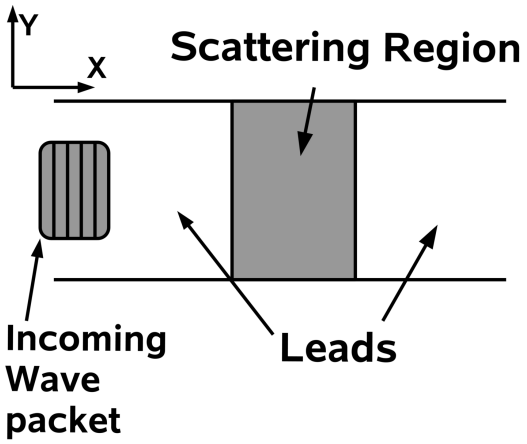

Figure 3.3: The wire is divided into three regions. One scattering region, which represents the nanostructure, and two leads.

In the scattering region the nanostructure will be represented by a scattering potential V_{sc} which will be added to the parabolic wire Hamiltonian in equation (3.1) to make up the total Hamiltonian for the system

$$H = \frac{\vec{\pi}^2}{2m^*} + \frac{1}{2}m^*\Omega_0 y^2 + V_{sc}(x,y). \tag{3.16}$$

The leads are the asymptotic limits of the scattering potential and there the total Hamiltonian can be replaced by the parabolic wire Hamiltonian. The Hamiltonian in equation (3.16) will be treated in the same way as the one in equation (3.1). This will give us a similar equation as equation (3.12) but with a projection of the scattering potential added on the right side,

$$\left\{(k_n(\omega)a_w)^2 - (qa_w)^2\right\}\varphi_n(q,\omega) = \sum_{n'}\int \frac{dpa_w}{\sqrt{2\pi}}U_{nn'}(q,p)\varphi_{n'}(q,y) \tag{3.17}$$

where,

$$U_{nn'}(q,p) = \frac{2\Omega_w}{a_w\hbar\Omega_0^2}\int dy\Phi_n^*(y-y_0(p))V(p-q,y)\Phi_{n'}(y-y_0(q)), \tag{3.18}$$

and $V(p-q,y)$ is the Fourier transform of $V_{sc}(x,y)$. Here we should note that the shifted eigenfunctions of the harmonic oscillator are only orthogonal if they are equally

shifted. At this point it is convenient to introduce the Greens function of the parabolic wire which is defined as

$$\left\{(k_n(\omega)a_w)^2 - (qa_w)^2\right\} G_n(q,\omega) = 1 \tag{3.19}$$

or

$$G_n(q,\omega) = \frac{1}{(k_n(\omega)a_w)^2 - (qa_w)^2}. \tag{3.20}$$

We can see from equation (3.12) that the Green function fullfills the relation,

$$\left\{(k_n a_w)^2(\omega) - (qa_w)^2\right\} \varphi_n^0(q,\omega) = G_n^{-1}(q,\omega)\varphi_n^0(q,\omega) = 0. \tag{3.21}$$

By using this Green function the solution to equation (3.17) can be written as

$$\varphi_n(q,\omega) = \varphi_n^0(q,\omega) + G_n(q,\omega)\sum_{n'}\int \frac{dpa_w}{\sqrt{2\pi}} U_{nn'}(q,p)\varphi_{n'}(p,\omega). \tag{3.22}$$

Equation (3.22) is a set of coupled integral equations called the Lippmann-Schwinger equations [18]. We will solve it by symbolically iterating it to all orders and define a new quantity which will only depend on the system but not on the wave function. This can be carried out as

$$\varphi = \varphi^0 + GU\varphi = \varphi^0 + GU\varphi^0 + GUGU\varphi^0 + \ldots = (1 + GT)\varphi^0, \tag{3.23}$$

where $T = U + UGT$ is an integral equation for the new quantity called the "T-matrix". This iteration can be thought of as representing all possible repetitions of scattering. That is to say the first term represents the incoming wave going through unscattered, the second term represents one scattering event, the third term two and etc. We solve the exact equation for the T-matrix in the momentum space

$$T_{nn'}(q,p,\omega) = U_{nn'}(q,p) + \sum_m \int \frac{dka_w}{\sqrt{2\pi}} U_{nm}(q,k)G_m(k,\omega)T_{mn'}(k,p,\omega). \tag{3.24}$$

The matrix elements in the T-matrix represent the weight of a scattering for energy $\hbar\omega$ from a momentum p in energy band n' to a momentum q in energy band n. How we calculate the T-matrix numerically is shown in Appendix A. In those calculations all orders of scattering are included which allows us to use scattering regions with complex geometry and structure. With the T-matrix we see that the solution to equation (3.22) is

$$\varphi_n(q,\omega) = \varphi_n^0(q,\omega) + G_n(q,\omega)\sum_{n'}\int \frac{dpa_w}{\sqrt{2\pi}} T_{nn'}(q,p,\omega)\varphi_{n'}^0(p,\omega), \tag{3.25}$$

which will give us the total wave function in coordinate space

$$\begin{aligned}
\Psi(x,y,t) &= \int \frac{dq}{\sqrt{2\pi}} \int \frac{d\omega}{\sqrt{2\pi}} e^{i(qx-\omega t)} \Psi(q,y,\omega) \\
&= \int \frac{dq}{\sqrt{2\pi}} \int \frac{d\omega}{\sqrt{2\pi}} e^{i(qx-\omega t)} \sum_n \varphi_n(q,\omega)\Phi_n(y-y_0(q)) \\
&= \int \frac{dq}{\sqrt{2\pi}} \int \frac{d\omega}{\sqrt{2\pi}} e^{i(qx-\omega t)} \sum_n \\
&\times \left(\varphi_n^0(q,\omega) + G_n(q,\omega) \sum_{n'} \int \frac{dp a_w}{\sqrt{2\pi}} T_{nn'}(q,p,\omega)\varphi_{n'}^0(p,\omega) \right) \Phi_n(y-y_0(q)). \\
&= \Psi_0(x,y,t) + \Psi_{sc}(x,y,t) \qquad (3.26)
\end{aligned}$$

Here we see that the total wave function after the incoming wave function enters the scattering region consists of the original incoming wave function plus a new scattered wave function $\Psi_{sc}(x,y,t)$ emanating from the scattering center.

3.4 Transport of a wave packet through the nanostructure

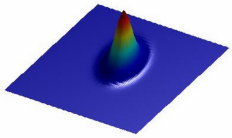

Figure 3.4: Wavepacket with a gaussian shape in the x direction.

We want to see how an electron or a short burst of electrons will travel through the nanostructure. To represent it we will use a gaussian shaped wave packet traveling in one energy band from the left lead. In equations (3.15) and (3.14) we have the formulas for the wave packet in the leads before it enters the scattering region. In order to get the Gaussian shape in the x direction as an initial condition we choose a Gaussian weight curve over the momentum

$$g_n(p) = \delta_{nm} e^{-\lambda(p-p_0)^2}, \qquad (3.27)$$

where λ is positive and controls the width of the wave packet in the x direction and p_0 is the momentum which the packet is centered around. With this initial condition we can calculate equation (3.15) directly, these calculations are shown in Appendix C. But for now we are more interested in equation (3.14). By using the property of the delta function [19]

$$\delta[f(x)] = \sum_j \frac{\delta(x-x_j)}{f'(x_j)} \qquad (3.28)$$

where $f(x_j) = 0$, we can represent equation (3.14) in two ways. The former representation is the original frequency representation

$$\varphi_n^0(p,\omega) = 2\pi g_n(p)\delta\left[\omega - \left(\frac{E_n}{\hbar} + \frac{a_w^2}{2}\frac{\Omega_0^2}{\Omega_w}p^2\right)\right] \qquad (3.29)$$

while the latter representation is a momentum representation

$$\varphi_n^0(p,\omega) = 2\pi g_n(p)\frac{\Omega_w}{\Omega_0^2|k_n(\omega)a_w|}\delta[pa_w - k_n(\omega)a_w]. \tag{3.30}$$

In equation (3.30) we construct the Gaussian weight function in such a way that the negative momentum contributions can be neglected. By inserting equation (3.29) into the former term in equation (3.26) we get the initial wave packet. But when we insert equation (3.30) into the latter term in equation (3.26) we get the scattering part of the wave function

$$\begin{aligned}\Psi_{sc}(x,y,t) &= \sum_{n'}\int_{\frac{E_{n'}}{\hbar}}^{\infty} d\omega e^{-i\omega t}\frac{\Omega_w g_{n'}(k_{n'}(\omega))}{\Omega_0^2|k_{n'}(\omega)a_w|} \\ &\times \sum_{n}\int_{-\infty}^{\infty}\frac{dqa_w}{\sqrt{2\pi}}G_n(q,\omega)e^{iqx}T_{nn'}\Big(q,k_{n'}(\omega),\omega\Big)\Phi_n(y-y_0(q)).\end{aligned} \tag{3.31}$$

Here the lower limit in the ω integration only goes down to $E_{n'}/\hbar$. Lower limits would correspond to imaginary momentum which would give evanescent terms in the initial wave packet, terms which we assume are non existing in the leads. Evanescent terms are though present in the scattering region through the Green function. By examining the Greens-function in equation (3.20) we see that is has two poles, $q = \pm k_n(\omega)$. We can use this fact to rewrite the q integral in equation (3.31) by expanding the integral into the complex plane and using the following relation

$$\lim_{\eta\to 0^+}\frac{1}{x \pm i\eta} = P\left(\frac{1}{x}\right) \mp i\pi\delta(x), \tag{3.32}$$

which we get from complex analysis[1]. This will result in a total wave function of the form

$$\begin{aligned}\Psi(x,y,t) &= \Psi_0(x,y,t) \\ &+ \sum_{n'}\int_{\frac{E_{n'}}{\hbar}}^{\infty}\frac{d\omega}{\sqrt{2\pi}}e^{-i\omega t}\frac{\Omega_w g_{n'}(k_{n'}(\omega))}{\Omega_0^2|k_{n'}(\omega)a_w|} \\ &\times \sum_{n}\Bigg[P\int_{-\infty}^{\infty}dq\frac{e^{iqx}T_{nn'}\Big(q,k_{n'}(\omega),\omega\Big)\Phi_n(y-y_0(q))}{(k_n(\omega)a_w)^2-(qa_w)^2} \\ &- \frac{i\pi}{2|k_n(\omega)a_w|}e^{ik_n(\omega)x}T_{nn'}\Big(k_n(\omega),k_{n'}(\omega),\omega\Big)\Phi_n(y-y_0(k_n(\omega))) \\ &- \frac{i\pi}{2|k_n(\omega)a_w|}e^{-ik_n(\omega)x}T_{nn'}\Big(-k_n(\omega),k_{n'}(\omega),\omega\Big)\Phi_n(y-y_0(-k_n(\omega)))\Bigg].\end{aligned} \tag{3.33}$$

[1] A more thorough approach of how to deal with the pole points that the Greens function introduces can be seen in Appendix A when dealing with calculations of the T-matrix.

The principal value integral in equation (3.33), which is the first term in the square brackets, represents scattering of free particle states into states which do not fullfill the free particle energy momentum relation of the leads, see equation (3.13). How much the energy momentum relation is violated is controlled by the Green function. Because these scattered states violate the energy momentum relation of the leads they are confined to the scattering region. The second and the third term within the square brackets of equation (3.33) represents on shell scattering which preserves the energy momentum relation of the leads. These scattered states can travel out of the scattering region. The states which the second term represents travel to the right while the states represented by the third term travel to the left. The integrals in equation (3.33) are calculated numerically with a repeated scheme of four point Gaussian integration.

3.5 Conductance through a nanostructure connected to a parabolic quantum wire

The conductance can be calculated for the static case which corresponds to a plane wave impinging on the scattering region. To calculate the conductance through the scattering region we will have to estimate how much of the incoming wave makes it through the right lead. Lets assume we are sending a planewave with energy $E = \hbar\omega_0$ from subband m into the scattering region. This will give us the following wave function in momentum and frequency space

$$\varphi_n^0(p,\omega) = 2\pi\delta_{nm}\delta(k_m(\omega_0) - p)\delta(\omega_0 - \omega). \tag{3.34}$$

When $\varphi_n^0(p,\omega)$, is used in equation (3.26) for the total wave function we get

$$\begin{aligned}\Psi(x,y,t) &= e^{ik_m(\omega_0)x - i\omega_0 t}\Phi_m(y - y_0(k_m(\omega_0))) \\ &+ \int \frac{dq}{\sqrt{2\pi}} e^{iqx - i\omega_0 t} \sum_n G_n(q,\omega_0) T_{nm}(q, k_m(\omega_0), \omega_0)\Phi_n(y - y_0(q)).\end{aligned} \tag{3.35}$$

We will now expand $\Psi(x,y,t)$ onto a base of shifted harmonic oscillators and use equation (3.32) to evaluate the q integral. This gives the coefficient function of the expansion as

$$\begin{aligned}\psi_n(x,t) &= e^{ik_m(\omega_0)x - i\omega_0 t}\delta_{nm} + P\int \frac{dq}{\sqrt{2\pi}} e^{iqx - i\omega_0 t} G_n(q,\omega_0) T_{nm}(q, k_m(\omega_0), \omega_0) \\ &- i\sqrt{\frac{\pi}{8}} \frac{e^{ik_n(\omega_0)x - i\omega_0 t}}{|k_n(\omega_0)a_w|} T_{nm}(k_n(\omega_0), k_m(\omega_0), \omega_0) \\ &- i\sqrt{\frac{\pi}{8}} \frac{e^{-ik_n(\omega_0)x - i\omega_0 t}}{|k_n(\omega_0)a_w|} T_{nm}(-k_n(\omega_0), k_m(\omega_0), \omega).\end{aligned} \tag{3.36}$$

The conductance depends on how much of the original wave is measured coming through the right lead. Now because the second term in equation (3.36) can not go outside the scattering region and the fourth term represents wave traveling to the left, these term will not contribute to the measured conductance. So the only terms that contributes are the first and the third terms. The right going part of the coefficient function is

$$\psi_n^R(x,t) = e^{ik_n(\omega_0)x - i\omega_0 t}\left\{\delta_{nm} - \sqrt{\frac{\pi}{8}}\frac{i}{|k_n(\omega_0)a_w|}T_{nm}(k_n(\omega_0), k_m(\omega_0), \omega_0)\right\}. \tag{3.37}$$

Thus a transmission matrix $t_{nm}(\omega_0)$ can be defined as

$$t_{nm}(\omega_0) = \delta_{nm} - \sqrt{\frac{\pi}{8}}\frac{i}{|k_n(\omega_0)a_w|}T_{nm}(k_n(\omega_0), k_m(\omega_0), \omega_0), \tag{3.38}$$

which can be interpreted as the probability for a planewave with energy $\hbar\omega_0$ to be transmitted forward into the right lead from energy band m into energy band n. Using this transmission matrix we can calculate the conductance for energy $\hbar\omega_0$ by using the Landauer formula

$$G(\omega_0) = G_0 \mathrm{Tr}[\mathbf{t}^\dagger(\omega_0)\mathbf{t}(\omega_0)] \tag{3.39}$$

where $G_0 = \frac{2e^2}{\hbar}$ is the double conductance quantum.

Chapter 4

Simulation of scattering in nanostructures

In this chapter we describe the results of the simulations of the scattering of a wave packet in nanostructures. Four types of potential structures will be studied, a constriction, a quantum ring, an acceptor-like impurity , and a donor-like impurity. We will study the quantum ring with various magnetic field strengths and the acceptor-like impurity with a wave packet from the first and second subbands. To get a picture of how a wave packet progresses through one of these nanostructures we have to solve equation (3.33) numerically for that particular nanostructure. The program which does these calculations has been implemented in Fortran90 with the ω integral programmed for parallel execution. Dimensions in the system have been scaled so the equations will suit better for numerical calculations. The scales used in the calculations are shown in table 4.1. In all the simulations the strength of the parabolic confinement potential is

Length	a_w
Wave Vector $\sim$ Momentum	a_w^{-1}
Time	$\hbar/\hbar\Omega_w$
Frequency	$\hbar\Omega_w/\hbar$

Table 4.1: Scales of the dimensions used in the numerical calculations.

fixed to $\hbar\Omega_0 = 1$ meV. This describes a broad quasi one-dimensional wire as apposed to one which is fully approximated as one-dimensional [7]. The wave packets are sent in with a momentum distribution centered around $k_0 = 2a_w^{-1}$. But because the magnetic length depends on the strength of the magnetic field this means that this center of momentum increases with strength of the magnetic field. In table 4.2 we see the magnetic field strengths used in the simulations, their corresponding magnetic lengths and initial center of momentum distribution of the wave packets. It should be noted that all the snapshots of the wave packets presented in this chapter has had their x-axis compressed and that their y-axis go from top to bottom.

$B[T]$	$a_w[nm]$	$k_0 = 2a_w^{-1}[nm^{-1}]$
0.2	32.8	0.061
0.3	31.8	0.063
0.5	29.3	0.068
2.0	17.8	0.11

Table 4.2: The corresponding effective magnetic lengths and initial centers of the momentum distribution of the wave packets for each of the magnetic fields used in the simulations.

4.1 Scattering through a constriction

We begin by using a constriction as our nanostructure, see figure (4.1). It is a simple structure and convenient for testing our model. To describe this constriction we will use the scattering potential

$$V_{\text{constriction}}(x, y) = Ve^{-\beta_x(x-\overline{x})^2-\beta_y y^2}, \tag{4.1}$$

where $V = 2$ meV, $\beta_x = 2 \cdot 10^{-5}$ nm^{-2}, $\overline{x} = 10a_w = 318$ nm, and $\beta_y = 2 \cdot 10^{-6}$ nm^{-2}. A magnetic field $B = 0.3$ T will be applied to the system and the four lowest energy bands are included in the calculations. In figure 4.2 we can see the conductance of the

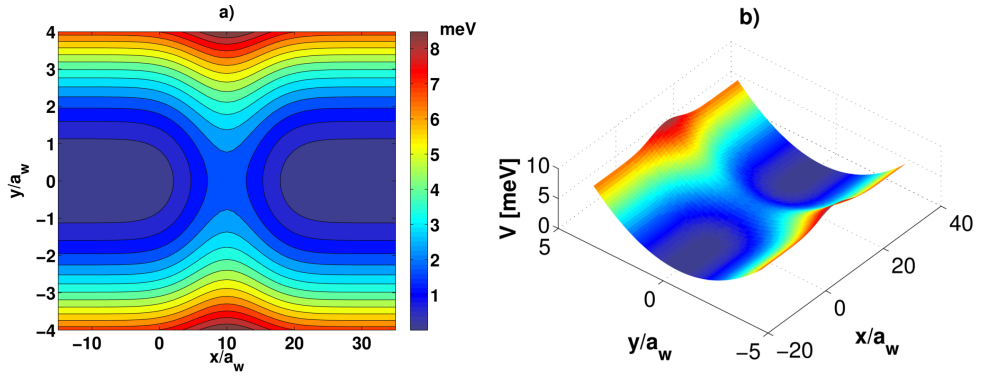

Figure 4.1: a) Contour plot of the constriction potential in the wire. b) 3D plot of the same potential in the wire.

system plotted as a function of energy. As a reference the weight function of the plane waves which are used to construct the initial wave packet is plotted as a function of energy. The simulation can be seen in figures 4.4 and 4.5 in section 4.1.1, where the former figure is a top view of the wave packet and the latter is a 3D view of the same wave packet. There we see the wave packet colliding onto the constriction and splitting into two wave packets as expected, one reflected and one transmitted. We also note that the center of the rightgoing incoming and transmitted packets are shifted to positive

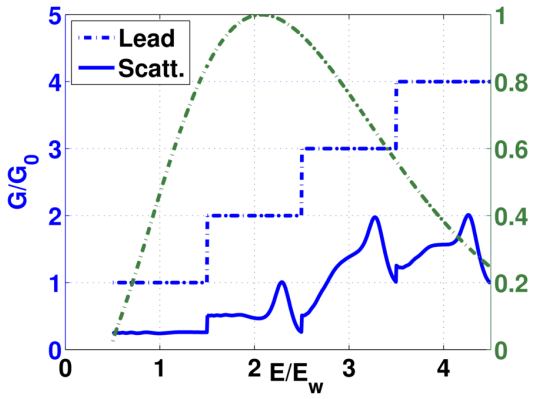

Figure 4.2: Conductance through the the leads and the scattering region containing the constriction as a function of energy for $B = 0.3$ T. As a reference the weight function of energy in the initial wave packet is also included (seen in green).

y-values, but the center of the leftgoing reflected packet is shifted to negative y-values due to the Lorentz force. Since a wave packet contains contribution with different momenta the Lorentz force also distorts the shape of a wave packet. But the transmitted wave packet seems to ripple and have two or more peaks. This could be explained by looking at the conductance graph in figure 4.2. There we see that the initial wave packet is mainly constructed out of energies which contain three conductance tops at 2.3 E_w, 3.3 E_w, and 4.3 E_w. Because the outcoming wave packets seems to mostly scatter back into the first subband of the leads the energy difference of these peaks in the conductance would result in higher kinetic energy of the more energetic peaks. These conductance peaks thus should show themselves in the transmitted wave packet as tops moving at different speeds, as seems to be the case in the simulations, see figure 4.3.

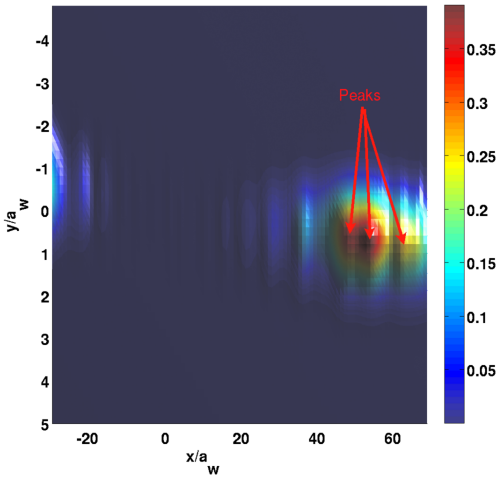

Figure 4.3: A snapshot of the wave packet shown at 28.7 ps with the peaks pointed out.

4.1.1 Snapshots of the wave packet traveling through a constriction

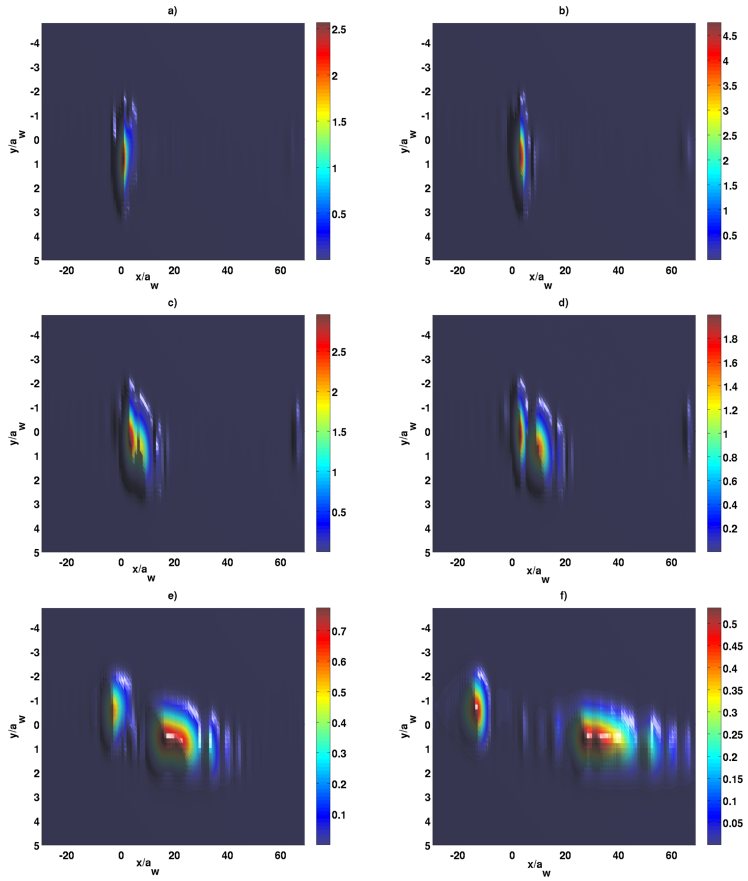

Figure 4.4: Top view of the wave packet traveling through a constriction at a) 0 ps, b) 1.24 ps, c) 3.12 ps, d) 4.36 ps, e) 9.99 ps, and f) 16.8 ps in $B = 0.3$ T magnetic field.

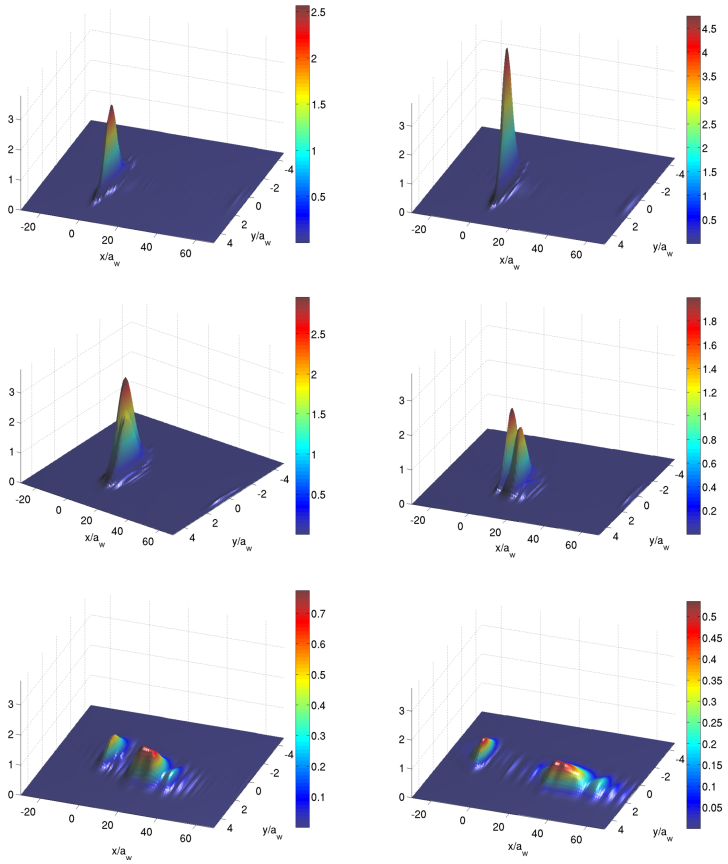

Figure 4.5: 3D view of the wave packet traveling through a constriction at a) 0 ps, b) 1.24 ps, c) 3.12 ps, d) 4.36 ps, e) 9.99 ps, and f) 16.8 ps in $B = 0.3$ T magnetic field.

4.2 Scattering through a quantum ring

Next we will turn our attention to a more complex structure. We will pick a nanostructure which looks like a circular trench with a peak in the middle, see figure 4.6. This will be our quantum ring. The potential of the ring is described by the equation

$$V_{\text{ring}}(x,y) = V_1 e^{-\beta_1\left((x-\overline{x})^2+y^2\right)} + V_2 e^{-\beta_2\left((x-\overline{x})^2+y^2\right)} \tag{4.2}$$

where $V_1 = -12$ meV, $V_2 = 18$ meV, $\beta_1 = 6 \cdot 10^{-5}$ nm^2, $\beta_2 = 6 \cdot 10^{-4}$ nm^2, and $\overline{x} = 20a_w$. The evolution of wave packets in the first subband of the leads which are injected into the nanostructure will be examined for three magnetic field strengths $B = 0.2$ T, $B = 0.5$ T, and $B = 2$ T. Also a wave packet in the second subband of the leads was injected into the nanostructure at $B = 0.2$ T. The lowest eight energy bands were included for all these calculations. Graphs of the conductance as function of

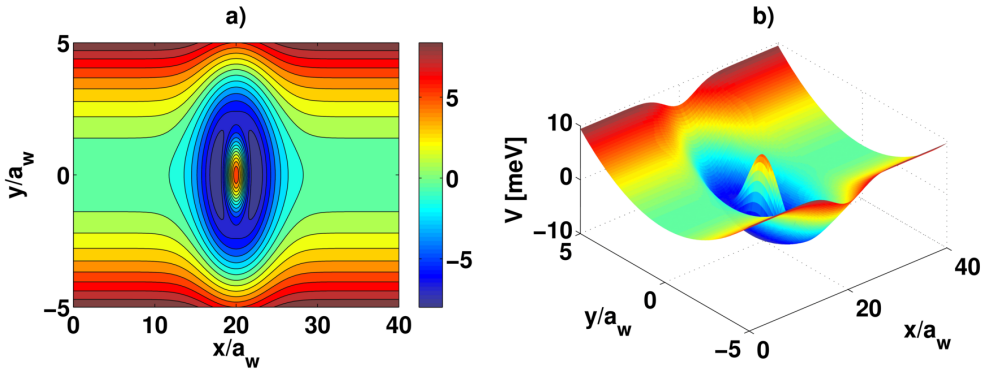

Figure 4.6: a) Contour plot of the quantum ring in the wire. b) 3D plot of the potential in the wire.

energy for each case can be seen in figure 4.8 and snapshots of the wave packets as they evolve through the quantum ring are shown in section 4.2.1. Lets begin by looking at the first two cases, that is to say electrons in states described by wave packets injected from the first energy subband into the quantum ring at magnetic strengths of $B = 0.2$ T and $B = 0.5$ T. The evolutions of these wave packets can be seen in figures 4.9 and 4.10 in section 4.2.1 for the case when $B = 0.2$ T, and figures 4.11 and 4.12 in the same section for the case when $B = 0.5$ T. There we see that the wave packets for each case evolve in a very similar way. Both are momentarily trapped in the quantum ring and are then scattered from it, leaving behind a weak circular quasi bound state which slowly leaks out into the left and the right leads [4]. An interesting thing to notice is that the reflected and transmitted wave packets perform a "zig zag" motion as they travel along the leads. This is shown better in figure 4.7 which is a snap shot from the case when the magnetic field strength is $B = 0.5$ T. This resembles the classical trajectories of electrons hopping along the wall of the leads in magnetic field or skipping orbits [20]. The only notable differences between these two cases are that we see the effects of the

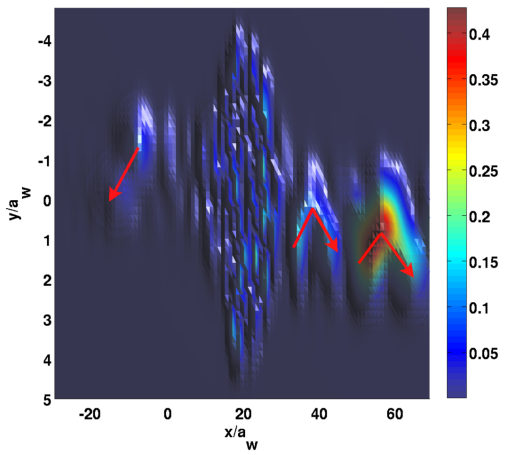

Figure 4.7: A snapshot of a wave packet evolving through a quantum ring with a $B = 0.5$ T magnetic field applied to it. The red arrows highlight the zig zag motion of the transmitted and the reflected packet.

Lorentz force more clearly for the $B = 0.5$ T case, as was expected, and the $B = 0.2$ T case seems to have a very little reflected wave packet. In the $B = 0.5$ T case we have a reflected wave packet of notable size which seems to move in the same zig zag way as the transmitted packet. But it is though considerably smaller than the transmitted packet. The difference in size of the reflected packets between the two cases could be explained by where they hit the quantum ring. The Lorentz force causes the wave packet to be further up the parabolic confinement potential for the case when $B = 0.5$ T than $B = 0.2$ T. This causes the wave packet in the $B = 0.5$ T case to hit the ring potential where it has more curvature along the y-axis than for the $B = 0.2$ T case, see figure 4.6, resulting that the wave packet in the 0.5 T case takes more circular path than for the $B = 0.2$ T case.
Lets next turn our attention to the case when the magnetic strength has been turned up to $B = 2.0$ T. Snapshots of the evolution of a wave packet in that case can be seen in figures 4.13 and 4.14 in section 4.2.1. There we see a very different scenario than from what we saw in the cases when $B = 0.2$ T and $B = 0.5$ T. The wave packet now gets more skewed than for lower magnetic field strengths as the Lorentz force pulls the faster high energy components higher up the parabolic potential. As the wave packet hits the quantum ring only a part of the packet seems to be affected by the quantum ring and we observe no visable backscattering. The lack of backscattering can be contributed to the large Lorentz force which makes it difficult for the wave packet to make a "U-turn" to the left. But the reason for why only a part of the wave packet is affected by the quantum ring depends on where the packet hits the ring. The lower energy components of the packet hit the ring where there is little or no circular curvature. So as the packet can not backscatter it has limited options other than to go straight ahead. But the more energetic components of the wave packet are higher up in

the parabolic potential and are confronted by more circular curvature which they can follow. In this case the Lorentz force also helps to direct these components into the curved path they take.
As our last case using the quantum ring we take a wave packet which is injected into the ring from the second subband of the leads and where the magnetic field strength is set to $B = 0.2$ T. In figures 4.15 and 4.16 in section 4.2.1 we see that the evolution of this wave packet is very similar to the case where a packet was injected from the first subband of the leads for $B = 0.2$ T. The packet is again trapped in the ring and leaves behind a circular semibound state as before. The packet seems though to spend more time at the quantum ring, which could be expected as this packet has lower kinetic energy than the one which was injected from the first energy level. The reflected and transmitted wave packet also shows a zig zag like movement as they scatter into the leads. It is interesting to see that the reflected and the transmitted packet seems to remain in the second energy level after scattering.

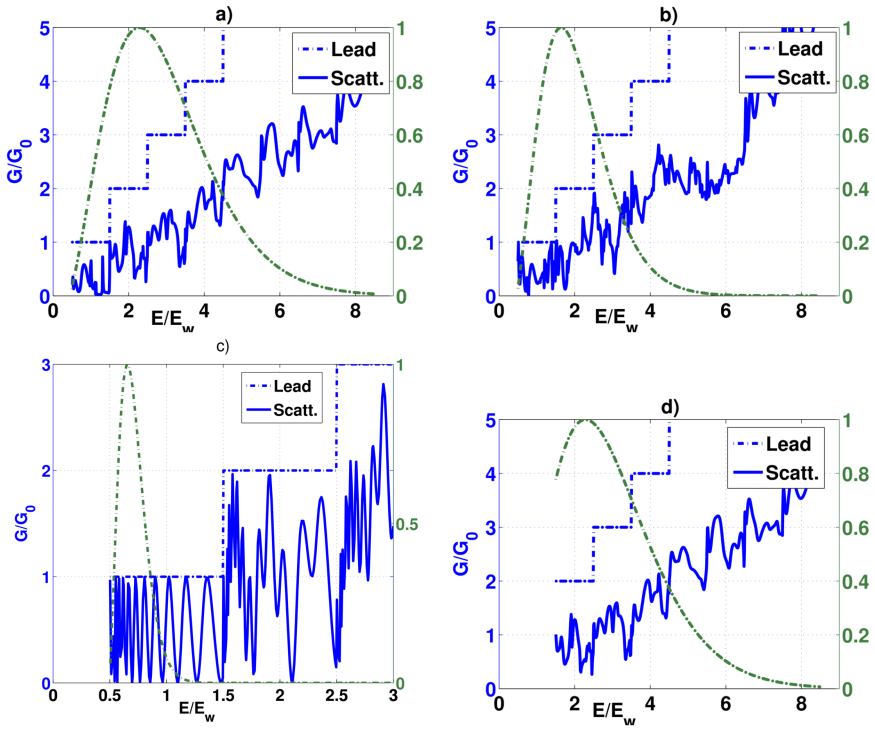

Figure 4.8: Conductance through the leads and the scattering region containing the quantum ring as a function of energy for a) $B = 0.2$ T, b) $B = 0.5$ T, c) $B = 2.0$ T, and d) $B = 0.2$ T. As a reference the weight function of energy in the initial wave packets is also included (seen in green). The weight function in a), b) and c) are for wave packet injected into the nanostructure from the first subband of the leads while the weight packet in d) is for a wave packet injected from the second subband. As the wave packet in d) is in the second subband energies in the initial wave packet do not go lower than 1.5 E_w.

4.2.1 Snapshots of the wave packet traveling through a quantum ring

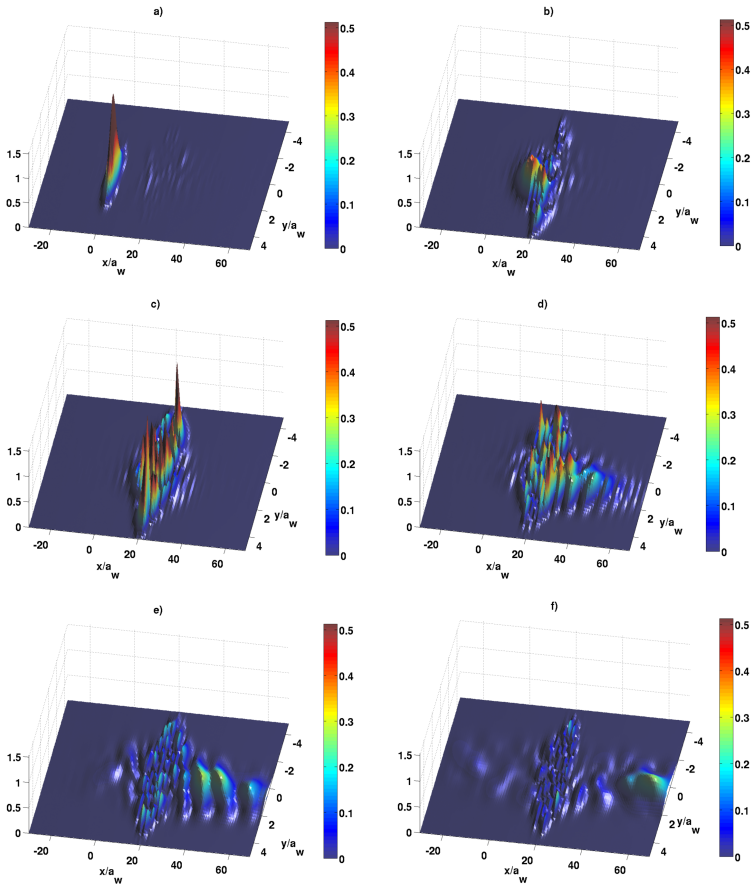

Figure 4.9: 3D view of a wave packet traveling through a quantum ring at a) 0 ps, b) 4.32 ps, c) 6.89 ps, d) 13.8 ps, e) 20.7 ps, f) 31.1 ps in $B = 0.2$ T magnetic field.

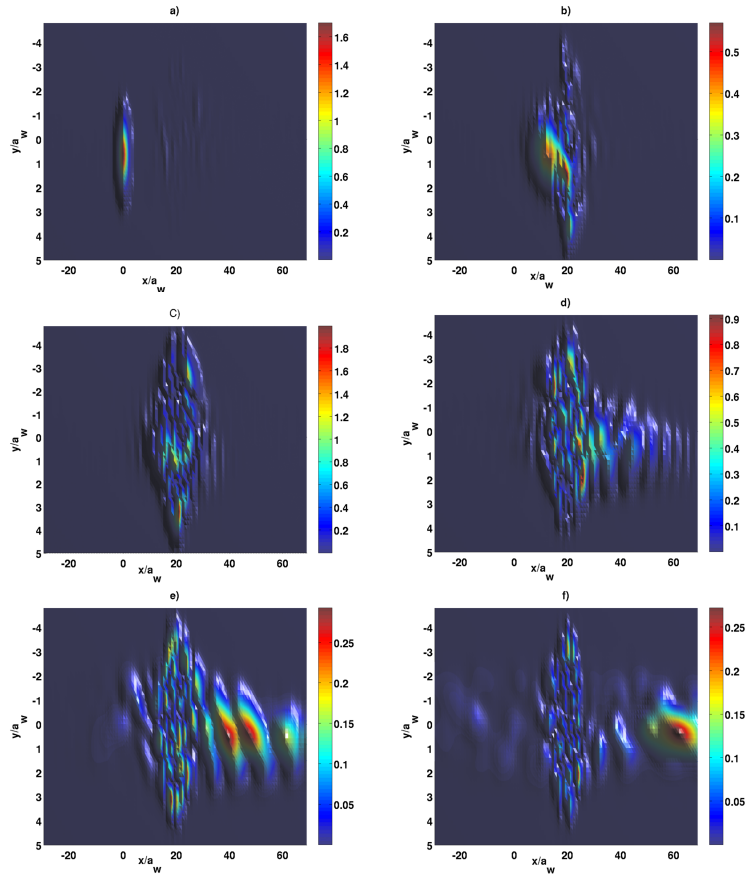

Figure 4.10: Top view of a wave packet traveling through a quantum ring at a) 0 ps, b) 4.32 ps, c) 6.89 ps, d) 13.8 ps, e) 20.7 ps, f) 31.1 ps in $B = 0.2$ T magnetic field.

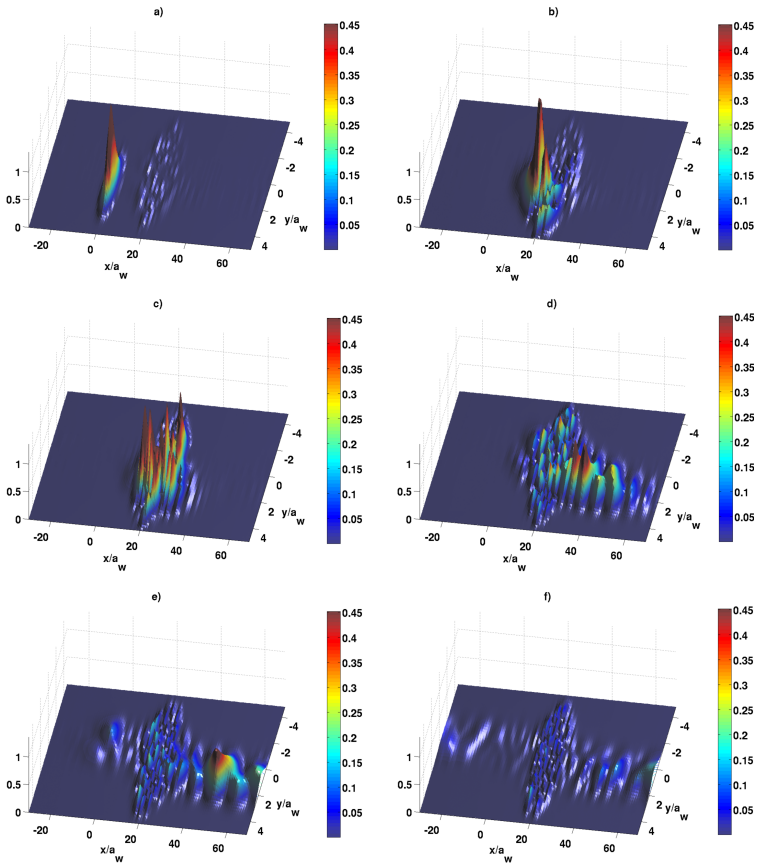

Figure 4.11: 3D view of a wave packet traveling through a quantum ring at a) 0 ps, b) 6.37 ps, c) 9.26 ps, d) 18.6 ps, e) 27.8 ps, f) 41.8 ps in $B = 0.5$ T magnetic field.

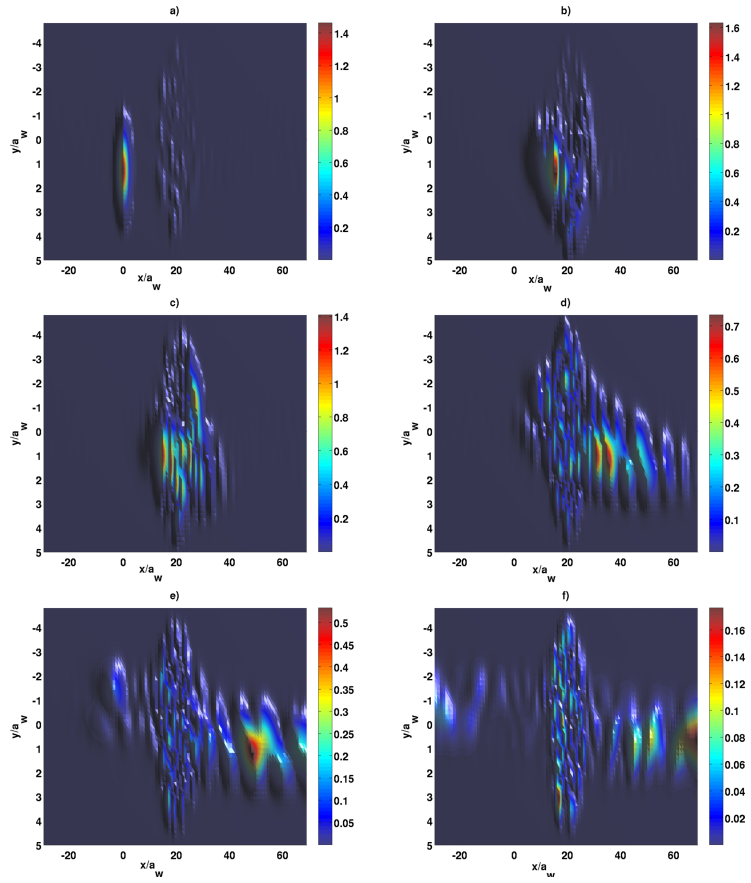

Figure 4.12: Top view of a wave packet traveling through a quantum ring at a) 0 ps, b) 6.37 ps, c) 9.26 ps, d) 18.6 ps, e) 27.8 ps, f) 41.8 ps in $B = 0.5$ T magnetic field.

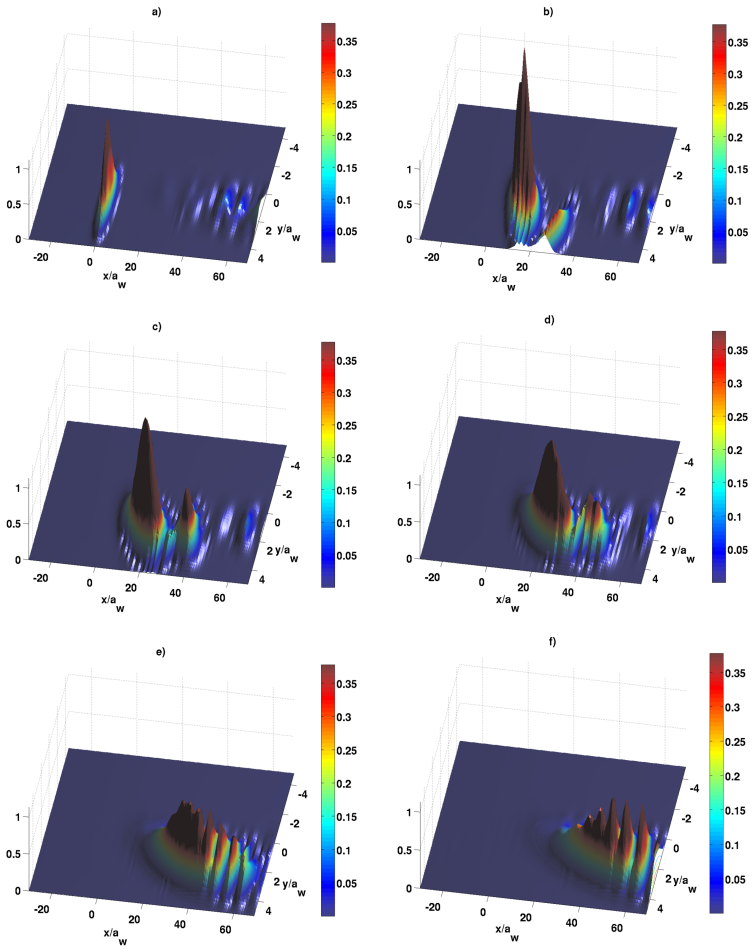

Figure 4.13: 3D view of a wave packet traveling through a quantum ring at a) 0 ps, b) 1.39 ps, c) 2.07 ps, d) 2.87 ps, e) 4.15 ps f) 5.54 ps in $B = 2.0$ T magnetic field.

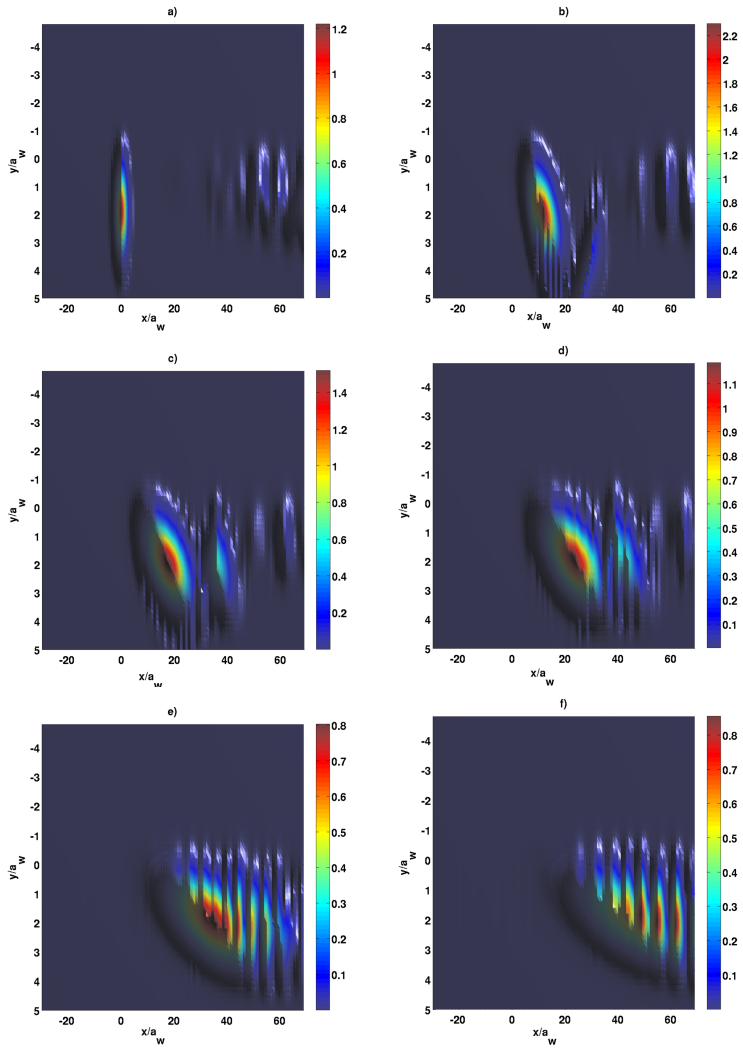

Figure 4.14: Top view of a wave packet traveling through a quantum ring at a) 0 ps, b) 1.39 ps, c) 2.07 ps, d) 2.87 ps, e) 4.15 ps f) 5.54 ps in $B = 2.0$ T magnetic field.

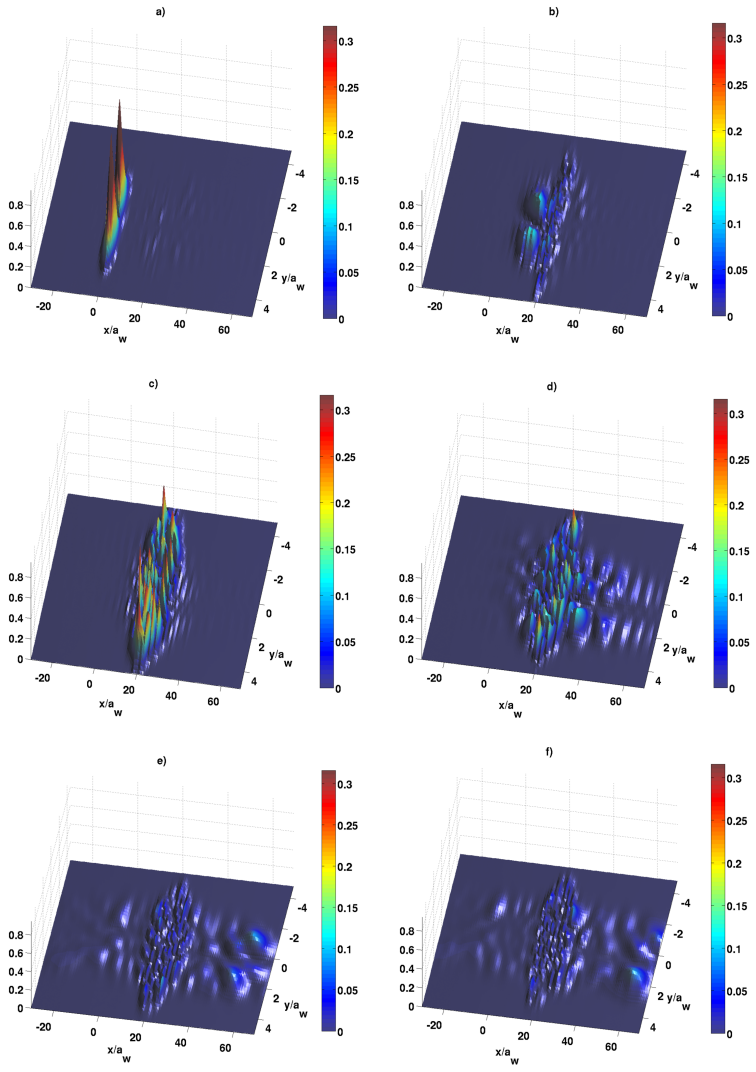

Figure 4.15: 3D view of a wave packet traveling through a quantum ring at a) 0 ps, b) 4.32 ps, c) 6.89 ps, d) 15.6 ps, e) 28.6 ps, f) 32.0 ps in $B = 0.2$ T magnetic field and injected from the second subband of the leads.

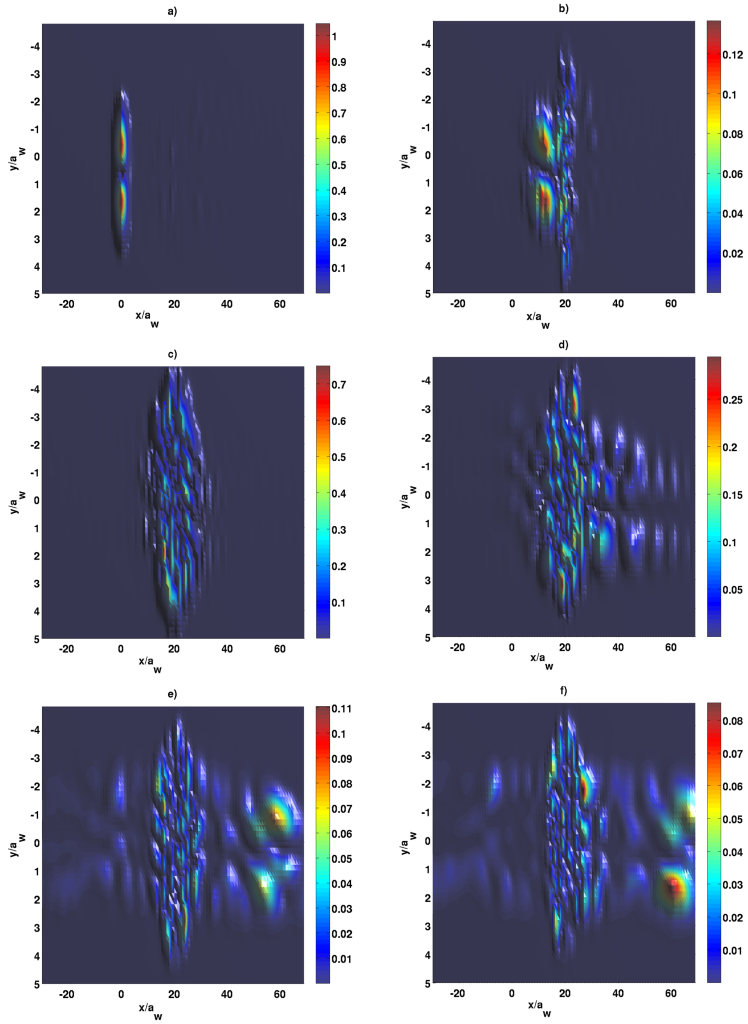

Figure 4.16: Top view of a wave packet traveling through a quantum ring at a) 0 ps, b) 4.32 ps, c) 6.89 ps, d) 15.6 ps, e) 28.6 ps, f) 32.0 ps in $B = 0.2$ T magnetic field and injected from the second subband of the leads.

4.3 Scattering through an acceptor-like impurity

Now we will look at a potential in the wire representing an acceptor-like impurity, see figure 4.17, and apply a magnetic strength of $B = 0.5$ T to the system. The potential is described by the equation

$$V_{\text{acceptor}}(x, y) = Ve^{-\beta\left((x-\overline{x})^2+y^2\right)}, \tag{4.3}$$

where $V = 8$ meV, $\beta = 1.0 \cdot 10^{-2}$ nm^{-2}, and $\overline{x} = 20a_w = 586$ nm. The six lowest energy bands where included for the simulations for this system. We will look at two

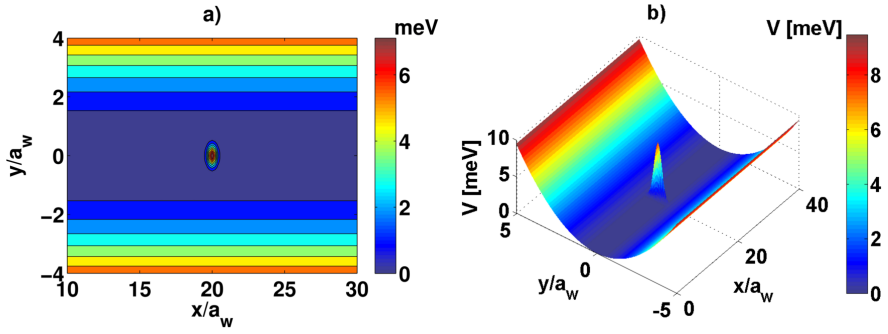

Figure 4.17: a) Contour plot of an acceptor-like impurity potential in the wire. b) 3D plot of the same potential in the wire.

cases for this system. One where we introduce a wave packet from the first subband of the leads, see figures 4.20 and 4.21 in section 4.3.1, and another where we introduce a wave packet from the second subband of the leads, see figures 4.22 and 4.23 in section 4.3.1. The static conductance through the leads and the scattering region as a function of energy along with weight function of energy in the initial wave packet can be seen in figure 4.19 for both cases. Lets begin by considering the case where the initial wave packet is in the first subband. What we see in figures 4.22 and 4.23 is the wave packet colliding into the impurity. The front of the wave packet, which is the most energetic part of it, seems to go through without much interaction with the potential. But the rest of the wave packet seems to be more effected by the potential and shows the zig zag motion as seen for other potentials. This results in that the transmitted packet seems to have a wiggling tale. A small reflected packet is also visable and displays a zig zag motion and lags in time as is seen for other potentials. We can notice a faint mode mixing at the potential as a part of the wave packet jumps from the first subband into an evanescent state in the second subband [21]. But no quasi bound state seems to have resulted after the scattering process as has been shown for higher magnetic field strengths in the static case [22, 23].
The case where the wave packet is initially in the second subband of the leads gives similar results as for the former case. It remains in the same subband after scattering as it was before scattering, which is the same result as we got for the quantum ring.

The main difference is that the packet shows a stronger mode mixing at the potential where a part of the packet jumps from the second subband to the third, see figure 4.18. An another thing to notice is that here are also no visible quasi bound states left at the potential as the reflected and transmitted packets leave it.

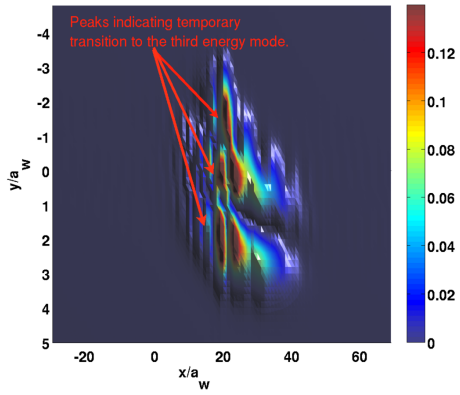

Figure 4.18: A top view of the wave packet at 13.7 ps. Here the three tops of the third subband evanescent state are pointed out.

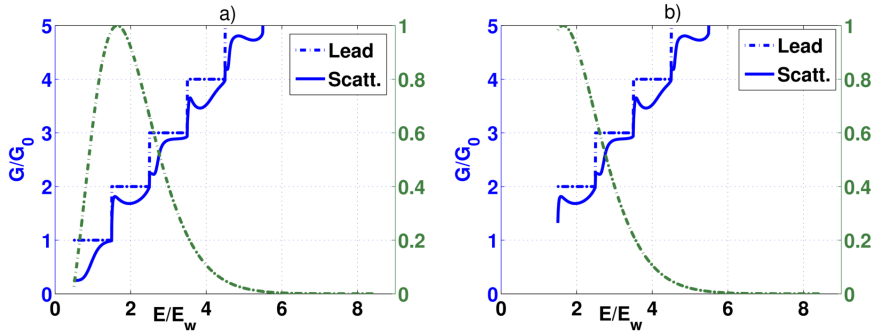

Figure 4.19: The static conductance through the leads and the acceptor-like impurity, a) with energy weight function for an initial wave packet from the first subband of the leads (seen in green), b) with energy weight function for an initial wave packet from the second subband of the leads (seen in green).

4.3.1 Snapshots of the wave packet traveling through an acceptor-like impurity

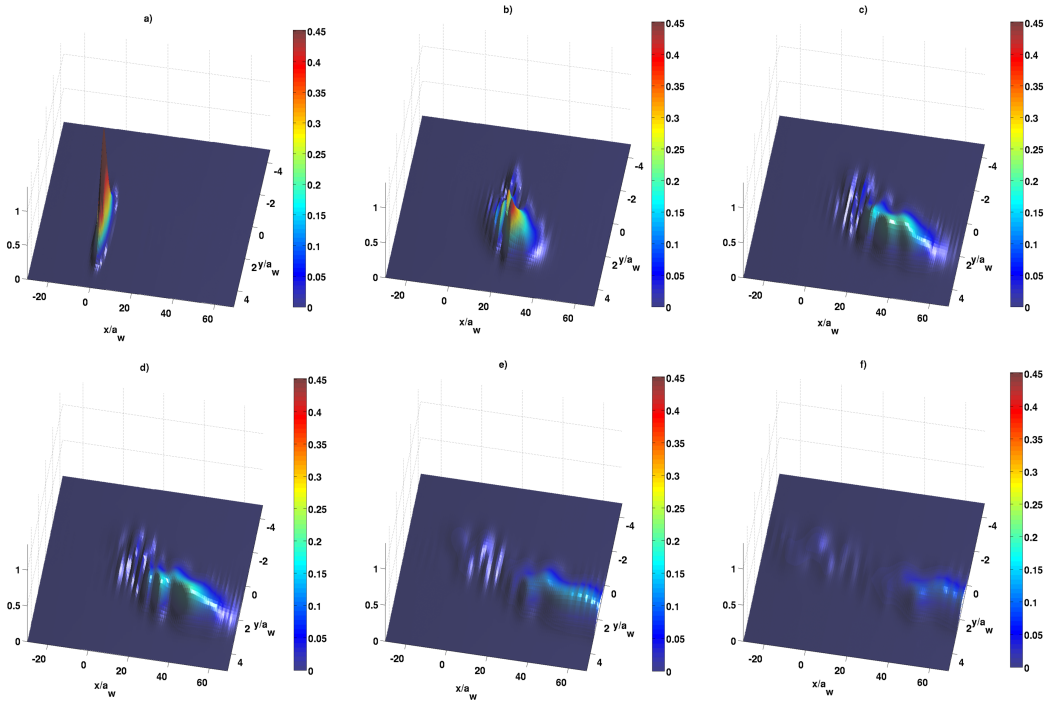

Figure 4.20: 3D view of a wave packet traveling through an acceptor-like impurity at a) 0 ps, b) 13.0 ps, c) 21.7 ps, d) 23.9 ps, e) 32.5 ps, f) 43.4 ps in $B = 0.5$ T magnetic field.

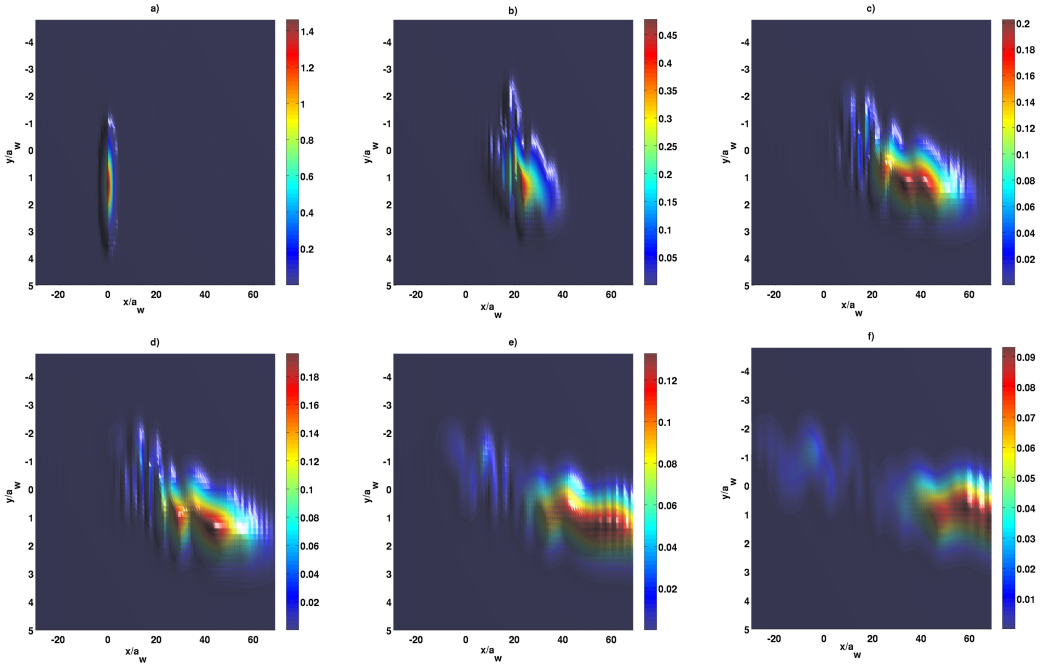

Figure 4.21: Top view of a wave packet traveling through an acceptor-like impurity at a) 0 ps, b) 13.0 ps, c) 21.7 ps, d) 23.9 ps, e) 32.5 ps, f) 43.4 ps in $B = 0.5$ T magnetic field.

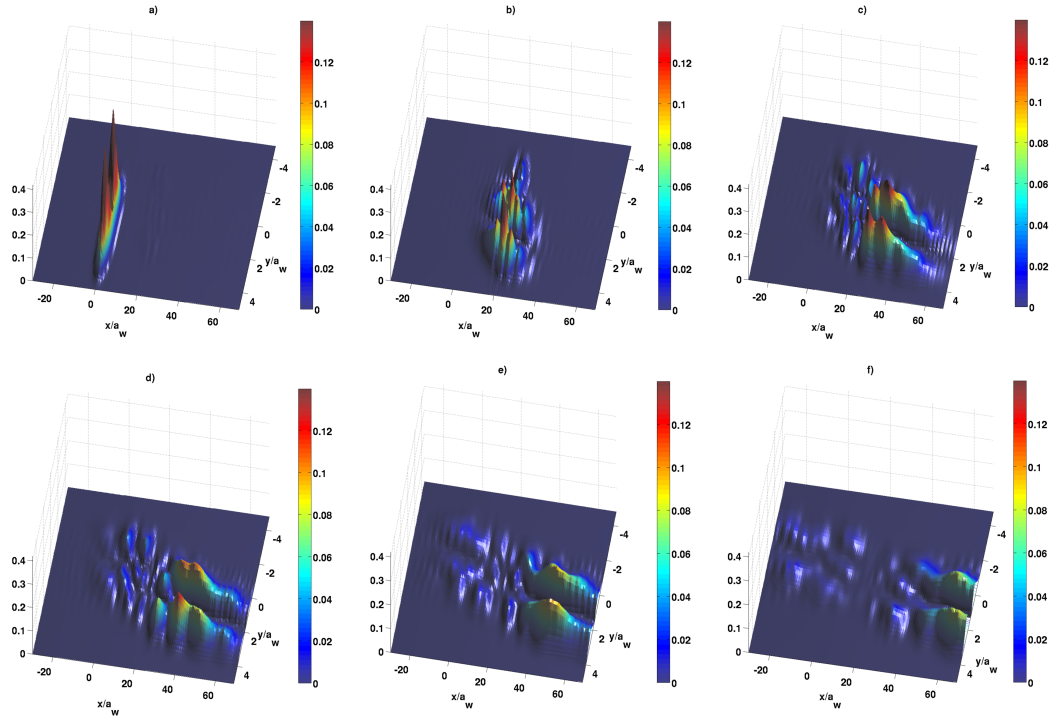

Figure 4.22: 3D view of a wave packet, injected from the second subband, traveling through an acceptor-like impurity at a) 0 ps, b) 10.9 ps, c) 21.7 ps, d) 26.8 ps, e) 32.5 ps, f) 43.4 ps in $B = 0.5$ T magnetic field.

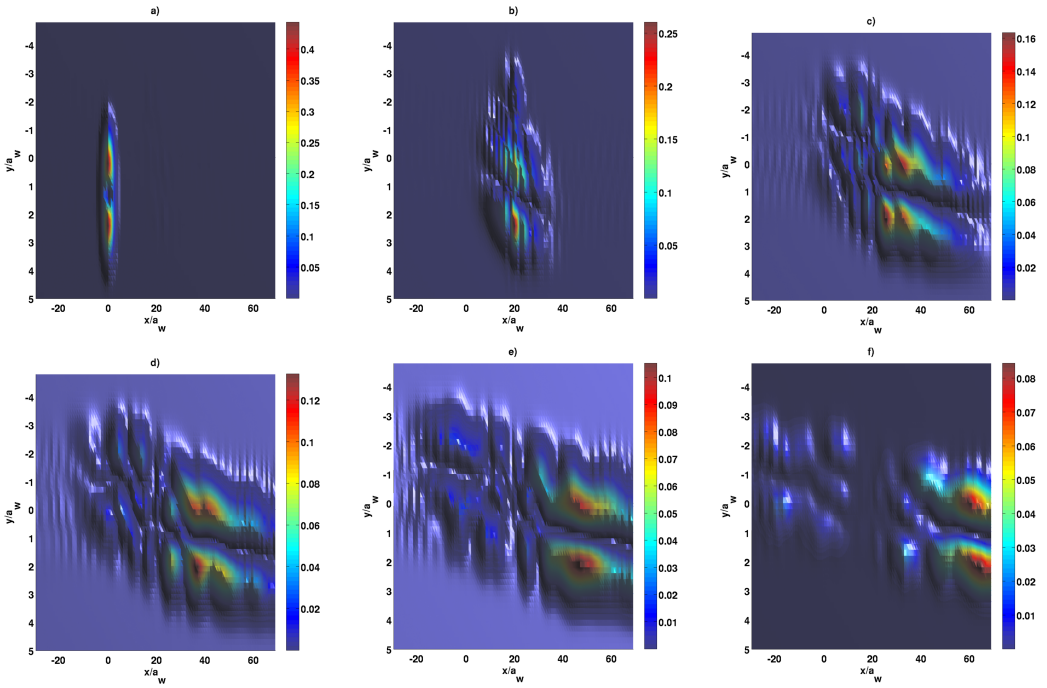

Figure 4.23: Top view of a wave packet, injected from the second subband, traveling through an acceptor-like impurity at a) 0 ps, b) 10.9 ps, c) 21.7 ps, d) 26.8 ps, e) 32.5 ps, f) 43.4 ps in $B = 0.5$ T magnetic field.

4.4 Scattering through a donor-like impurity

As our last nanostructure we will pick a narrow potential well representing a donor-like impurity, see figure 4.27 applied with a magnetic strength of $B = 0.5$ T. The potential is described as

$$V_{\text{donor}}(x, y) = Ve^{-\beta\left((x-\overline{x})^2+y^2\right)} \tag{4.4}$$

where $\beta = 1.0 \cdot 10^{-2}$ nm^{-2}, $\overline{x} = 20a_w = 586$ nm, and the depth is $V = -8$ meV. The six lowest energy bands were included for this simulations as was done for the acceptor.

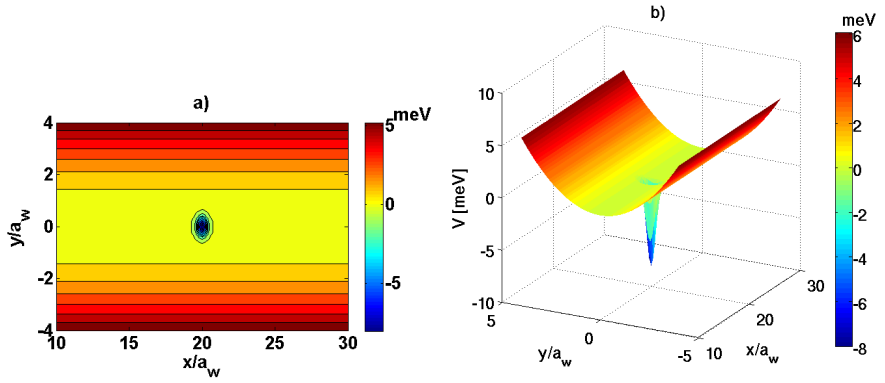

Figure 4.24: a) Contour plot of a donor-like potential in the wire. b) 3D plot of the same potential in the wire.

This potential is really just an inverse of the acceptor we examined in section 4.3. In figure 4.25 we can see the static conductance graph for the donor and in figures 4.26 and 4.27 in section 4.4.1 we can see snapshots of the wave packet as it travels through donor. In the snapshots we see that the wave packet evolves in a similar way as it did for the acceptor. We see a mode mixing as a part of the packet jumps from the first subband into an evanescent state in a second subband, a transmitted packet with a wiggling tale, and a small reflected packet. But we can also detect a weak quasi bound state left behind after the scattered packets leave the scattering area. This is something we did not see for the acceptor. The magnetic field breaks the parity with respect to the y direction allowing a transition to the second subband. Without the magnetic field this transition would be forbidden [3].

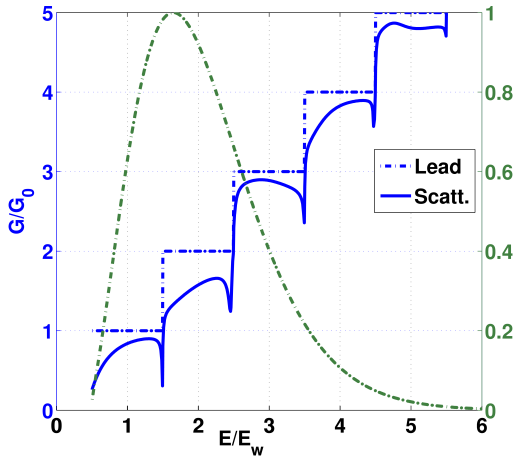

Figure 4.25: Static conductance through the leads and scattering region containing the donor-like impurity as a function of energy with the weight function of energies in the initial wave packet (seen in green).

4.4.1 Snapshots of the wave packet traveling through a donor-like impurity

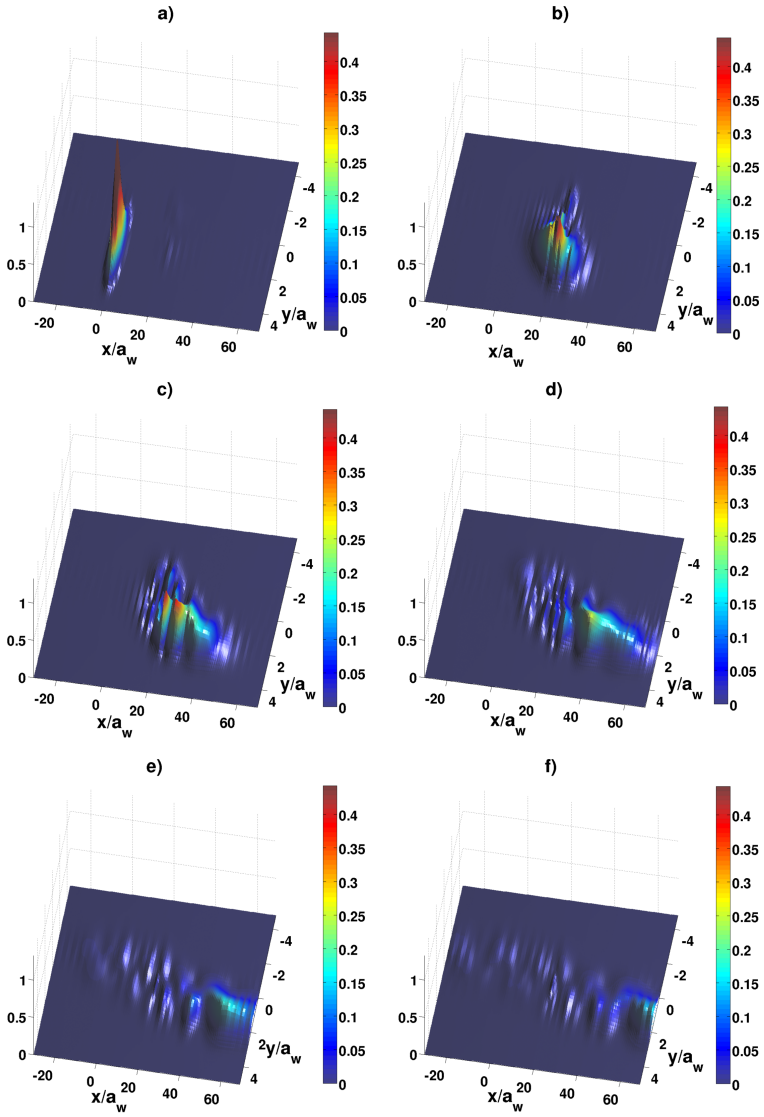

Figure 4.26: 3D view of a wave packet, injected from the second subband, traveling through a donor-like impurity at a) 0 ps, b) 8.72 ps, c) 13.9 ps, d) 19.7 ps, e) 28.4 ps, f) 34.8 ps in $B = 0.5$ T magnetic field.

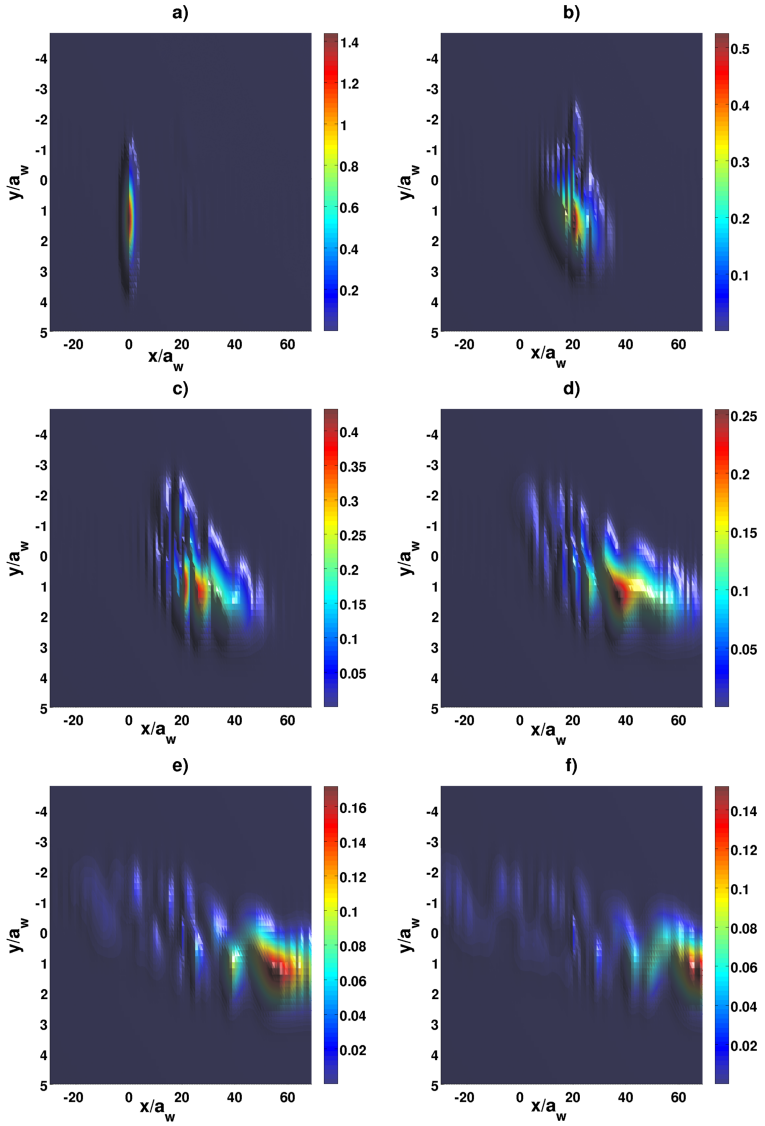

Figure 4.27: Top view of a wave packet, injected from the second subband, traveling through a donor-like impurity at a) 0 ps, b) 8.72 ps, c) 13.9 ps, d) 19.7 ps, e) 28.4 ps, f) 34.8 ps in $B = 0.5$ T magnetic field.

Chapter 5

Summary

In this thesis a model of a time dependent evolution of an electron wave packet traveling through a quantum wire with an embedded nanostructure has been presented. The model is built upon the Lippmann-Schwinger formalism [18] for scattering theory and is capable of handling any nanostructure which can be represented by a sum of Gaussian potentials covering a finite area in an infinite parabolic quantum wire. The model was applied to four different embedded nanostructures: a constriction (which was used as a basic test for the model), quantum ring, an acceptor-like impurity, and a donor-like impurity. The system is held in a perpendicular homogeneous magnetic field. By applying an idea developed by Gurvitz [1] the Lippmann-Schwinger equation is transformed into momentum-coordinate space where it can be separated in spite of the magnetic field.

Of these structures the quantum ring was most extensively tested, applying to it three different magnetic field strengths and injecting wave packets into it from two different subbands of the leads. The wave packet showed a very regular circular form when entering the quantum ring for all cases except the case where a high magnetic field was applied. Also in all cases, except the high magnetic one, the wave packet left behind a quasi bound state after scattering. The embedded potential representing an acceptor-like impurity was hit by wave packets from the first and second subband of the leads. As the wave packet from the first subband entered the scattering region it was observed that a small part of it jumped from the first subband into a short lived evanescent state in the second subband. This kind of mode mixing was more obvious for the wave packet entering from the second subband as a large part of it jumped from the second subband into an evanescent state in the third subband. The reason for that the mode mixing is more apparent for the wave packet in the second subband than the one in the first subband is propably because the wave packet entering from the second subband has lower kinetic energy than the one entering from the first subband. It therefore spends more time in the scattering region and is more affected by the scattering potential. No quasi bound state living for an extended time were observed for the acceptor-like impurity in the magnetic field used in the simulation. One simulation was performed for the donor-like impurity and it showed similar results as for the ac-

ceptor, except that a faint quasi bound state was observed. For all the transmitted and reflected wave packets that scattered from the nanostructures used in the simulations, except for the constriction, some kind of a zig zag motion was observed. This zig zag motion represents the electron jumping on the wall of the leads or skipping orbits. Also for all the simulations a time lag for different parts of the packets was observed as the wave packets scattered from the embedded nanostructures. This time lag was seen to be greater for the reflected wave packets than the transmitted.
With comparison to the static case [3,4,21,22] the results from these simulations indicate that this model gives a realistic picture of the evolution of a wave packet through quantum wires with embedded nanostructures. It has also sheds light on features not apparent in the static case, such as time lags. We have thus developed a general model for describing the passage of electron wave packets through quantum nanostructures of finite width. Combined with the result from the static conductance calculations, and the investigations on transient effects in transport [9] the future is now open for research into signal processing in nanosystems.

Appendix A

Numerical calculations of the T-matrix

This section will be devoted to transform the equation for the T-matrix,

$$T_{nn'}(q,p,\omega) = U_{nn'}(q,p) + \sum_m \underbrace{\int \frac{dka_w}{\sqrt{2\pi}} U_{nm}(q,k) G_m(k,\omega) T_{mn'}(k,p,\omega)}_{I_m}, \tag{A.1}$$

from a linear integral equation into a linear algebra equation [24] in section 3.3. When we examine equation (3.20) we notice that for fixed energy the Green function has two poles, $k = \pm k_n(\omega)$. To calculate the integral I_m we have to get rid of these poles [25]. So we expand our calculations from the real axis onto the complex plane. The path which we will integrate over on the complex plane will form a semicircle as seen in figure (A.1)

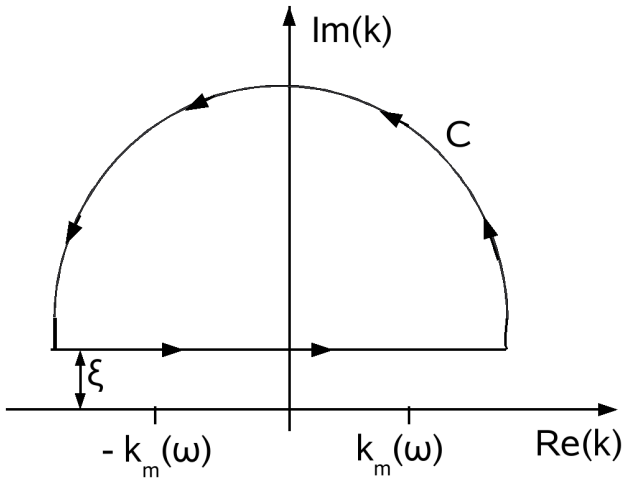

Figure A.1: The integration contour in the complex plane.

Now because $U_{nm}(q,k)$ and $G_m(k,\omega)$ go to zero as $|k| \to \infty$ it is safe to assume that $T_{mn'}(k,p,\omega)$ goes to zero as well when $|k| \to \infty$. This means that we can expand the semi-circle in figure (A.1) to infinity and make use of the Jordan's Lemma. So the only term of the

integral which gives us a contribution is the path of the integral parallel to the real axis

$$\begin{aligned} I_m &= \oint_C \frac{dka_w}{\sqrt{2\pi}} U_{nm}(q,k) G_m(k,\omega) T_{mn'}(k,p,\omega) \\ &= \lim_{\xi\to 0^+} \int_{-\infty}^{\infty} \frac{dka_w}{\sqrt{2\pi}} \frac{U_{nm}(q,k) T_{mn'}(k,p,\omega)}{(k_m(\omega)a_w)^2 - (ka_w)^2 + i\xi}. \end{aligned} \tag{A.2}$$

With a help from a well known relation in complex analysis,

$$\lim_{\xi\to 0^+} \frac{1}{x \pm i\xi} = P\left(\frac{1}{x}\right) \mp i\pi\delta(x),$$

along with equation (3.28) in section 3.4, which tells us how to rewrite the delta function, we can rewrite the integral I_m as

$$\begin{aligned} I_m &= \underbrace{P\int_{-\infty}^{\infty} \frac{dka_w}{\sqrt{2\pi}} \frac{U_{nm}(q,k) T_{mn'}(k,p,\omega)}{(k_m(\omega)a_w)^2 - (ka_w)^2}}_{I_P} \\ &- \sqrt{\frac{\pi}{8}} \frac{i}{|k_m(\omega)a_w|} U_{nm}(q,-k_m(\omega)) T_{mn'}(-k_m(\omega),p,\omega) \\ &- \sqrt{\frac{\pi}{8}} \frac{i}{|k_m(\omega)a_w|} U_{nm}(q,k_m(\omega)) T_{mn'}(k_m(\omega),p,\omega). \end{aligned} \tag{A.3}$$

We could evaluate the principal value integral I_P in equation (A.3) directly as

$$\begin{aligned} I_P &= \pm i\sqrt{\frac{\pi}{8}} \frac{U_{nm}(q,k_m(\omega)) T_{mn'}(k_m(\omega),p,\omega) - U_{nm}(q,-k_m(\omega)) T_{mn'}(-k_m(\omega),p,\omega))}{k_m(\omega)a_w} \\ &+ \sqrt{2\pi} i \sum \text{Res}[U_{nm}(q,k) T_{mn'}(k,p,\omega)]. \end{aligned} \tag{A.4}$$

but as we do not know the residues of the T-matrix beforehand equation (A.4) is of little practical use to us. We therefore have to evaluate the principal value integral I_P numerically. The first step to achieve that goal is to turn the principal value integral into a regular integral [2]. That is to say, we have to make it continuous over the pole points. By using the fact that

$$P\int_{-\infty}^{\infty} dx \frac{1}{y^2 - x^2} = P\int_{-\infty}^{\infty} dx \frac{1}{2y}\left(\frac{1}{x-y} - \frac{1}{x+y}\right) = 0 = 2P\int_0^{\infty} dx \frac{1}{y^2 - x^2} \tag{A.5}$$

we can rewrite I_P as

$$\begin{aligned} I_P &= \int_0^{\infty} \frac{dka_w}{\sqrt{2\pi}} \frac{U_{nm}(q,-k) T_{mn'}(-k,p,\omega) - U_{nm}(q,-k_m(\omega)) T_{mn'}(-k_m(\omega),p,\omega)}{(k_m(\omega)a_w)^2 - (ka_w)^2} \\ &+ \int_0^{\infty} \frac{dka_w}{\sqrt{2\pi}} \frac{U_{nm}(q,k) T_{mn'}(k,p,\omega) - U_{nm}(q,k_m(\omega)) T_{mn'}(k_m(\omega),p,\omega)}{(k_m(\omega)a_w)^2 - (ka_w)^2}. \end{aligned} \tag{A.6}$$

If $\lim_{k\to\infty} d/dk U_{nm}(q,\pm k) T_{mn'}(\pm k,p,\omega)$ is finite we can add again to the integral the points which contained the poles without reintroducing the poles. This can be confirmed by l'Hôpital's

rule. To integrate the I_P integral numerically we will use a repeated four point Gaussian integration schema [26]. If $g(k)$ is our integrand we will rewrite and approximate the integral as

$$\begin{aligned}\int_0^\infty \frac{dk}{\sqrt{2\pi}} g(k) &\approx \int_0^{k_{max}} \frac{dk}{\sqrt{2\pi}} g(k) = \sum_{n_G=1}^{N_G} \int_{(n_g-1)\Delta}^{n_g\Delta} \frac{dk}{\sqrt{2\pi}} g(k) \\ &\approx \sum_{n_G=1}^{N_G} \frac{\Delta}{\sqrt{8\pi}} \sum_{i=1}^{4} v_i g\left(\frac{\Delta}{2}(t_i + 2n_g - 1)\right) \\ &= \sum_{n_G=1}^{N_G} \frac{\Delta}{\sqrt{8\pi}} \sum_{i=1}^{4} v_i g(\tau_i(n_g)) \end{aligned} \tag{A.7}$$

where $\tau_i(n_g) = \Delta(t_i + 2n_g - 1)/2$. Here we have put an upper limit on the integral and divided it into N_G parts on the momentum axis, each of size Δ. Each part is then integrated by a four point Gaussian integration. The Gauss points t_i and weights v_i are given by table A.1.

i	t_i	v_i
1	-0.86113631	0.34785485
2	-0.33998104	0.65214515
3	0.33998104	0.65214515
4	0.86113631	0.34785485

Table A.1: Points and their corresponding weights used in four point Gaussian integration for scaled integrals.

Now if we also limit the number of energy bands to m_{max}, we get a numerical version of equation (A.1), which is

$$\begin{aligned} & T_{nn'}(q,p,\omega) \approx U_{nn'}(q,p) + \sum_{m=0}^{m_{max}} \\ \times & \left[\frac{\Delta a_w}{\sqrt{8\pi}} \sum_{n_G=1}^{N_G} \sum_{i=1}^{4} v_i \frac{U_{nm}(q,-\tau_i(n_g))T_{mn'}(-\tau_i(n_g),p,\omega) - U_{nm}(q,-k_m(\omega))T_{mn'}(-k_m(\omega),p,\omega)}{(k_m(\omega)a_w)^2 - (\tau_i(n_g)a_w)^2} \right. \\ + & \frac{\Delta a_w}{\sqrt{8\pi}} \sum_{n_G=1}^{N_G} \sum_{i=1}^{4} v_i \frac{U_{nm}(q,\tau_i(n_g))T_{mn'}(\tau_i(n_g),p,\omega) - U_{nm}(q,k_m(\omega))T_{mn'}(k_m(\omega),p,\omega)}{(k_m(\omega)a_w)^2 - (\tau_i(n_g)a_w)^2} \\ - & \left. \sqrt{\frac{\pi}{8}} \frac{i}{|k_m(\omega)a_w|} \{U_{nm}(q,k_m(\omega))T_{mn'}(k_m(\omega),p,\omega) + U_{nm}(q,-k_m(\omega))T_{mn'}(-k_m(\omega),p,\omega)\} \right]. \end{aligned} \tag{A.8}$$

To simplify things we trade off the double sum $\sum_{n_G=1}^{N_G} \sum_{i=1}^{4}$ for a simple sum $\sum_{l=1}^{N}$ where $l = 4(n_g - 1) + i$ and $N = 2N_G$. Now lets count τ and v in this new way, that is $\tau_i(n_g) \to \tau_l$

and $v_i \to v_l$,[1] and make a new Gauss net κ_l that expand over both negative and positive τ's, see table A.2.

	$l = 1, \ldots, \frac{N}{2}$	$l = \frac{N}{2} + 1, \ldots, N$
κ_l	$-\tau_{\frac{N}{2}-l+1}$	$\tau_{l-\frac{N}{2}}$

Table A.2: New integration net based on the four point Gaussian integration schema.

Using this new Gauss net equation (A.8) will give us

$$\begin{aligned} T_{nn'}(q,p,\omega) = U_{nn'}(q,p) &+ \frac{\Delta a_w}{\sqrt{8\pi}} \sum_{m=1}^{m_{max}} \sum_{l=1}^{N} v_l \frac{U_{nm}(q,\kappa_l) T_{mn'}(\kappa_l,p,\omega)}{(k_m(\omega)a_w)^2 - (\kappa_l a_w)^2} \\ - \frac{\Delta a_w}{\sqrt{32\pi}} &\sum_{m=1}^{m_{max}} \sum_{l=1}^{N} v_l \frac{U_{nm}(q,k_m(\omega)) T_{mn'}(k_m(\omega),p,\omega) + U_{nm}(q,-k_m(\omega)) T_{mn'}(-k_m(\omega),p,\omega)}{(k_m(\omega)a_w)^2 - (\kappa_l a_w)^2} \\ - \sum_{m=1}^{m_{max}} &\sqrt{\frac{\pi}{8}} \frac{i}{|k_m(\omega)a_w|} \{U_{nm}(q,k_m(\omega)) T_{mn'}(k_m(\omega),p,\omega) + U_{nm}(q,-k_m(\omega)) T_{mn'}(-k_m(\omega),p,\omega)\}. \end{aligned} \tag{A.9}$$

Equation (A.9) presents a form for the T-matrix which is convenient for numerical calculations. But it is still an implicit equation which could be solved with iteration. But we would like to avoid to constrict ourself to finite iterations and would like calculate a T which is to all orders. This can be achieved by turning equation (A.9) into a simple linear algebra equation. Lets begin by once again expanding our Gauss net to a new net k_j which includes all energy bands upp to m_{max} and add the poles points $\pm k_m(\omega)$ in each band. The procedure for this expansion can be seen in table A.3 where $N_{bands}(m) = (N+2)m$.

	$j = N_{bands}(m)+1, \ldots, N_{bands}(m)+N$	$j = N_{bands}(m)+N+1$	$l = N_{bands}(m)+N+2$
k_j	$\kappa_{j-N_{bands}(m)}$	$-k_m(\omega)$	$k_m(\omega)$

Table A.3: An expanded integration net containing points in all energy bands, including the pole points.

Using this net we can define a vector $D(k_j)$ as

$$D(k_j) = \begin{cases} \frac{\Delta a_w}{\sqrt{8\pi}} \frac{v_j}{(k_m(\omega)a_w)^2 - (k_j a_w)^2} & \text{for} \quad k_j \neq \pm k_m(\omega) \\ -\frac{\Delta a_w}{\sqrt{32\pi}} \sum_{l=1}^{2N} \frac{v_j}{(k_m(\omega)a_w)^2 - (k_j a_w)^2} - \sqrt{\frac{\pi}{8}} \frac{i}{|k_m(\omega)a_w|} & \text{for} \quad k_j = \pm k_m(\omega). \end{cases}$$

With this $D(k_j)$ vector along by replacing the continuous variables p and q by the discreet nets $\{k_r\} = \{k_j\}$ and $\{k_s\} = \{k_j\}$ we can rewrite equation (A.9) as

$$T(k_s,k_r,\omega) = U(k_s,k_r) + \sum_{j=1}^{N_{bands}(m_{max})} U(k_s,k_j)\, D(k_j) T(k_j,k_r,\omega)\,. \tag{A.10}$$

[1] Here all the n_g cells have identical list of v_l.

By defining a matrix

$$F(k_s, k_j) = \delta_{k_j,k_s} - U\left(k_s, k_j\right) D(k_j) \tag{A.11}$$

and use it to rewrite equation (A.10) we finally get the simple linear algebra equation which we were aiming at,

$$\sum_{j=1}^{m_{max}(2N+2)} F(q, k_j) T\left(k_j, p, \omega\right) = U(q, p). \tag{A.12}$$

As is obvious from equation (A.12) we can now calculate a solution for the T-matrix that is to all orders of scattering.

Appendix B

Calculations of the matrix elements of the embedded potential

The scattering potentials that are used in the numerical calculations are made of sums of Gaussian potentials written as

$$V(x,y) = \sum_t V_t e^{-\beta_{xt}(x-\overline{x}_t)^2 - \beta_{yt}(y-\overline{y}_t)^2}. \tag{B.1}$$

in real space. Here V_t is the strength of the potential number t, $\overline{x}_t$ and $\overline{y}_t$ give the position of the top of the potential while β_{xt} and β_{yt} control how wide the Gaussian potential is in the x and y directions. In our calculations in section 3.3 we first projected the scattering potential onto a plane wave space and then onto a space of shifted harmonic wavefunctions. Lets do that for the Gaussian potentials.

$$\begin{aligned} V_{nn'}(q,p) &= \langle n|V|n'\rangle = \sum_t V_t \int_{-\infty}^{\infty} \frac{dx}{\sqrt{2\pi}} \int_{-\infty}^{\infty} dy e^{-ipx} \Phi_n^*(y-y_0(p)) V(x,y) \Phi_{n'}(y-y_0(q)) e^{iqx} \\ &= \sum_t V_t \underbrace{\int_{-\infty}^{\infty} \frac{dx}{\sqrt{2\pi}} e^{i(q-p)x - \beta_{xt}(x-\overline{x}_t)^2}}_{V_x} \underbrace{\int_{-\infty}^{\infty} dy \Phi_n^*(y-y_0(p)) e^{-\beta_{yt}(y-\overline{y}_t)^2} \Phi_{n'}(y-y_0(q))}_{V_y}, \end{aligned} \tag{B.2}$$

where $\Phi_n(y-y_0(q))$ is the shifted harmonic wavefunction written as [27]

$$\Phi_n(y-y_0(q)) = \frac{e^{-\frac{1}{2}\left(\frac{y-y_0(q)}{a_w}\right)^2}}{\sqrt{2^n \pi^{1/2} n! a_w}} H_n\left(\frac{y-y_0(q)}{a_w}\right). \tag{B.3}$$

As can be seen from equation (B.2) the x and y integrals can be calculated separately. We begin by calculating the x-integral which is the simpler of the two [28]:

$$\begin{aligned} V_x &= \int_{-\infty}^{\infty} \frac{dx}{\sqrt{2\pi}} e^{-\beta_{xt}(x-\overline{x}_t)^2 - i(p-q)x} \overbrace{=}^{x'=x-\overline{x}_t} \frac{e^{-i(p-q)\overline{x}_t}}{\sqrt{2\pi}} \int_{-\infty}^{\infty} dx' e^{-\beta_{xt}x'^2 - i(q-p)x'} \\ &= \frac{1}{\sqrt{2\beta_{xt}}} e^{-\frac{(p-q)^2}{4\beta_{xt}}} = \frac{a_w}{\sqrt{2\beta_{xt}a_w^2}} e^{-i(pa_w - qa_w)\frac{\overline{x}_t}{a_w} - \frac{(pa_w - qa_w)^2}{4\beta_{xt}a_w^2}}. \end{aligned} \tag{B.4}$$

Next we will calculate the y integral. By inserting equation (B.3) into equation (B.2) we get

$$\begin{aligned} V_y &= \frac{1}{\sqrt{2^{n+n'}\pi n!n'!}}\int_{-\infty}^{\infty}\frac{dy}{a_w}e^{-\frac{1}{2}\left(\frac{y-y_0(p)}{a_w}\right)^2-\frac{1}{2}\left(\frac{y-y_0(q)}{a_w}\right)^2-\beta_{yt}a_w^2\frac{(y-\overline{y}_t)^2}{a_w^2}} \\ &\times H_n\left(\frac{y-y_0(p)}{a_w}\right)H_{n'}\left(\frac{y-y_0(q)}{a_w}\right) \end{aligned} \tag{B.5}$$

Now by rewriting the exponential in equation (B.5) as

$$\begin{aligned} & -\frac{1}{2}\left(\frac{y-y_0(p)}{a_w}\right)^2-\frac{1}{2}\left(\frac{y-y_0(q)}{a_w}\right)^2-\beta_{yt}a_w^2\left(\frac{y-\overline{y}_t}{a_w}\right)^2 \\ = & -(1+\beta_{yt}a_w^2)\left(\frac{y}{a_w}-\frac{\frac{y_0(p)}{a_w}+\frac{y_0(q)}{a_w}+2\beta_{yt}a_w^2\frac{\overline{y}_t}{a_w}}{2(1+\beta_{yt}a_w^2)}\right)^2 \\ + & \frac{\left(\frac{y_0^2(p)}{a_w^2}+\frac{y_0^2(q)}{a_w^2}+2\beta_{yt}a_w^2\frac{\overline{y}_0^2}{a_w^2}\right)^2}{4(1+\beta_{yt}a_w^2)}-\frac{1}{2}\left(\frac{y_0^2(p)}{a_w^2}+\frac{y_0^2(q)}{a_w^2}+2\beta_{yt}a_w^2\frac{\overline{y}_0^2}{a_w^2}\right) \end{aligned} \tag{B.6}$$

and making the following change of variables $y/a_w = S/(\sqrt{1+\beta_{yt}a_w^2})$ our V_y integral becomes

$$\begin{aligned} V_y &= \frac{\exp\left(\frac{1}{4(1+\beta_{yt}a_w^2)}\left(\frac{y_0(p)}{a_w}+\frac{y_0(q)}{a_w}+2\beta_{yt}a_w^2\frac{\overline{y}_t}{a_w}\right)^2-\frac{1}{2}\left(\frac{y_0^2(p)}{a_w^2}+\frac{y_0^2(q)}{a_w^2}+2\beta_{yt}a_w^2\frac{\overline{y}_0^2}{a_w^2}\right)\right)}{\sqrt{2^{n+n'}\pi n!n'!(1+\beta_{yt}a_w^2)}} \\ &\times \int_{-\infty}^{\infty}dS\exp\left[-\left(S-\frac{\frac{y_0(p)}{a_w}+\frac{y_0(q)}{a_w}+2\beta_{yt}a_w^2\frac{\overline{y}_t}{a_w}}{2\sqrt{1+\beta_{yt}a_w^2}}\right)^2\right] \\ &\times H_n\left(\frac{S}{\sqrt{1+\beta_{yt}a_w^2}}-\frac{y_0(p)}{a_w}\right)H_{n'}\left(\frac{S}{\sqrt{1+\beta_{yt}a_w^2}}-\frac{y_0(q)}{a_w}\right). \end{aligned} \tag{B.7}$$

We now use the following relation [28],

$$2^{\frac{n}{2}}H_n(x+y)=\sum_{i=0}^{n}\binom{n}{i}H_{n-i}\left(x\sqrt{2}\right)H_i\left(y\sqrt{2}\right). \tag{B.8}$$

to rewrite the Hermite polynomials in our integral,

$$\begin{aligned} V_y &= \frac{\exp\left(\frac{1}{4(1+\beta_{yt}a_w^2)}\left(\frac{y_0(p)}{a_w}+\frac{y_0(q)}{a_w}+2\beta_{yt}a_w^2\frac{\overline{y}_t}{a_w}\right)^2-\frac{1}{2}\left(\frac{y_0^2(p)}{a_w^2}+\frac{y_0^2(q)}{a_w^2}+2\beta_{yt}a_w^2\frac{\overline{y}_0^2}{a_w^2}\right)\right)}{\sqrt{2^{n+n'}\pi n!n'!(1+\beta_{yt}a_w^2)}} \\ &\times \sum_{i=0}^{n}\binom{n}{i}\sum_{j=0}^{n'}\binom{n'}{j}H_i\left(-\sqrt{2}\frac{y_0(p)}{a_w}\right)H_j\left(-\sqrt{2}\frac{y_0(q)}{a_w}\right) \\ &\times \int_{-\infty}^{\infty}dS\exp\left[-\left(S-\frac{\left(\frac{y_0(p)}{a_w}+\frac{y_0(q)}{a_w}+\beta_{yt}a_w^2\frac{\overline{y}_t}{a_w}\right)^2}{2\sqrt{1+\beta_{yt}a_w^2}}\right)^2\right] \\ &\times H_{n-i}\left(\sqrt{\frac{2}{1+\beta_{yt}a_w^2}}S\right)H_{n'-j}\left(\sqrt{\frac{2}{1+\beta_{yt}a_w^2}}S\right) \end{aligned} \tag{B.9}$$

The integral in equation (B.9) is known and has the following solution [28]

$$\int_{-\infty}^{\infty} dx e^{-(x-y)^2} H_m(\alpha x) H_n(\alpha x) = \pi^{1/2} \sum_{k=0}^{\min(m,n)} 2^k k! \binom{m}{k} \binom{n}{k} (1-\alpha^2)^{\frac{m+n}{2}-k} H_{m+n-2k}\left[\frac{\alpha y}{(1-\alpha^2)^{1/2}}\right], \tag{B.10}$$

which results in

$$\begin{aligned} V_y &= \frac{\exp\left(\frac{1}{4(1+\beta_{yt}a_w^2)}\left(\frac{y_0(p)}{a_w}+\frac{y_0(q)}{a_w}+2\beta_{yt}a_w^2\frac{\overline{y}_t}{a_w}\right)^2-\frac{1}{2}\left(\frac{y_0^2(p)}{a_w^2}+\frac{y_0^2(q)}{a_w^2}+2\beta_{yt}a_w^2\frac{\overline{y}_t^2}{a_w^2}\right)\right)}{\sqrt{2^{n+n'}\pi n!n'!(1+\beta_{yt}a_w^2)}} \\ &\times \sum_{i=0}^{n}\sum_{j=0}^{n'}\binom{n}{i}\binom{n'}{j} H_i\left(-\sqrt{2}\frac{y_0(p)}{a_w}\right) H_j\left(-\sqrt{2}\frac{y_0(q)}{a_w}\right) \sum_{k=0}^{\min(n-i,n'-j)} 2^k k! \binom{n-i}{k}\binom{n'-j}{k} \\ &\times \left(1-\frac{2}{1+\beta_{yt}a_w^2}\right)^{\frac{n-i+n'-j}{2}-k} H_{n-i+n'-j-2k}\left[\frac{\frac{y_0(p)}{a_w}+\frac{y_0(q)}{a_w}+2\beta_{yt}a_w^2\frac{\overline{y}}{a_w}}{\sqrt{2(1+\beta_{yt}a_w^2)^2-4(1+\beta_{yt}a_w^2)}}\right]. \end{aligned} \tag{B.11}$$

Now the y and x integrals have been calculated and by joining them together we get

$$\begin{aligned} V_{nn'}(q,p) &= \sum_t V_t \frac{a_w}{\sqrt{2\beta_{xt}a_w^2}} e^{-i(pa_w-qa_w)\frac{\overline{x}_t}{a_w}-\frac{(pa_w-qa_w)^2}{4\beta_{xt}a_w^2}} \\ &\times \frac{\exp\left(\frac{1}{4(1+\beta_{yt}a_w^2)}\left(\frac{y_0(p)}{a_w}+\frac{y_0(q)}{a_w}+2\beta_{yt}a_w^2\frac{\overline{y}_t}{a_w}\right)^2-\frac{1}{2}\left(\frac{y_0^2(p)}{a_w^2}+\frac{y_0^2(q)}{a_w^2}+2\beta_{yt}a_w^2\frac{\overline{y}_0^2}{a_w^2}\right)\right)}{\sqrt{2^{n+n'}\pi n!n'!(1+\beta_{yt}a_w^2)}} \\ &\times \sum_{i=0}^{n}\sum_{j=0}^{n'}\binom{n}{i}\binom{n'}{j} H_i\left(-\sqrt{2}\frac{y_0(p)}{a_w}\right) H_j\left(-\sqrt{2}\frac{y_0(q)}{a_w}\right) \sum_{k=0}^{\min(n-i,n'-j)} 2^k k! \binom{n-i}{k}\binom{n'-j}{k} \\ &\times \left(1-\frac{2}{1+\beta_{yt}a_w^2}\right)^{\frac{n-i+n'-j}{2}-k} H_{n-i+n'-j-2k}\left[\frac{\frac{y_0(p)}{a_w}+\frac{y_0(q)}{a_w}+2\beta_{yt}a_w^2\frac{\overline{y}}{a_w}}{\sqrt{2(1+\beta_{yt}a_w^2)^2-4(1+\beta_{yt}a_w^2)}}\right]. \end{aligned} \tag{B.12}$$

To use this in our calculations we remember that

$$U_{nn'}(q,p) = \frac{2}{\hbar a_w}\frac{\Omega_w}{\Omega_0^2} V_{nn'}(q,p) \tag{B.13}$$

Appendix C

Calculations of the initial wavepacket

In equation (3.15) in section 3.1 we have the solution for the wavefunction in the leads. The initial condition was chosen in equation (3.27) in section 3.4 to be

$$g_n(p) = \delta_{nm} e^{-\lambda(p-p_0)^2}. \tag{C.1}$$

Lets write $y_0(q) = a_w^2 y_0 q$, where $y_0 = \omega_c/\Omega_w$, and insert the initial condition in equation (C.1) into equation (3.15),

$$\begin{aligned}
\Psi_0(x,y,t) &= \int_{-\infty}^{\infty} dq g(q) e^{iqx} \Phi_m(y - y_0(q)) e^{-i\left(\frac{a_w^2}{2}\frac{\Omega_0^2}{\Omega_w}q^2 + \frac{E_m}{\hbar}\right)t} \\
&= \frac{1}{\sqrt{2^m \pi^{\frac{1}{2}} m! a_w}} \int_{-\infty}^{\infty} dq e^{-\left(\lambda^2 + \frac{a_w^2 y_0^2}{2} + i\frac{a_w^2}{2}\frac{\Omega_0^2}{\Omega_w}t\right)q^2 + \left(2\lambda^2 q_0 + y y_0 + ix\right)q - \lambda^2 q_0^2 - \frac{y^2}{2a_w^2} - i\frac{E_m}{\hbar}t} \\
&\times \quad H_m\left(\frac{y - a_w^2 y_0 q}{a_w}\right)
\end{aligned} \tag{C.2}$$

and do the following change of variables

$$q = \frac{y}{y_0 a_w^2} - \frac{k}{\sqrt{\lambda^2 + \frac{a_w^2 y_0^2}{2} + i\frac{a_w^2}{2}\frac{\Omega_0^2}{\Omega_w}t}} \tag{C.3}$$

where k is a dimensionless variable. This results in

$$\begin{aligned}
\Psi_0(x,y,t) &= \frac{-1}{\sqrt{2^m \pi^{\frac{1}{2}} m! a_w \left(\lambda^2 + \frac{a_w^2 y_0^2}{2} + i\frac{a_w^2}{2}\frac{\Omega_0^2}{\Omega_w}t\right)}} \\
&\times \int_{-\infty}^{\infty} dk \exp\left\{ -k^2 + \frac{\frac{2y}{y_0 a_w^2}\left(\lambda^2 + \frac{a_w^2 y_0^2}{2} + i\frac{a_w^2}{2}\frac{\Omega_0^2}{\Omega_w}t\right) - 2\lambda^2 q_0 - y y_0 - ix}{\sqrt{\lambda^2 + \frac{a_w^2 y_0^2}{2} + i\frac{a_w^2}{2}\frac{\Omega_0^2}{\Omega_w}t}} k \right. \\
&- \left. \frac{y^2}{y_0^2 a_w^4}\left(\lambda^2 + \frac{a_w^2 y_0^2}{2} + i\frac{a_w^2}{2}\frac{\Omega_0^2}{\Omega_w}t\right) + \frac{y}{y_0 a_w^2}\left(2\lambda^2 q_0 + y y_0 + ix\right) - \lambda^2 q_0^2 - \frac{y^2}{2a_w^2} - i\frac{E_m}{\hbar}t \right\}
\end{aligned}$$

$$\times \quad H_m\left(\frac{ka_w}{\sqrt{\frac{\lambda^2}{y_0^2}+\frac{a_w^2}{2}+i\frac{a_w^2}{2y_0^2}\frac{\Omega_0^2}{\Omega_w}t}}\right). \tag{C.4}$$

To simplify this equation we define four new variables;

$$A = \frac{-1}{\sqrt{2^m\pi^{\frac{1}{2}}m!a_w\left(\lambda^2+\frac{a_w^2y_0^2}{2}+i\frac{a_w^2}{2}\frac{\Omega_0^2}{\Omega_w}t\right)}}, \tag{C.5}$$

$$\begin{aligned}\xi &= \frac{\frac{2y}{y_0a_w^2}\left(\lambda^2+\frac{a_w^2y_0^2}{2}+i\frac{a_w^2}{2}\frac{\Omega_0^2}{\Omega_w}t\right)-2\lambda^2q_0-yy_0-ix}{\sqrt{\lambda^2+\frac{a_w^2y_0^2}{2}+i\frac{a_w^2}{2}\frac{\Omega_0^2}{\Omega_w}t}} \\ &= \frac{\left(\frac{2y}{y_0a_w^2}-2q_0\right)\lambda^2+i\left(\frac{y}{y_0}\frac{\Omega_0^2}{\Omega_w}t-x\right)}{\sqrt{\lambda^2+\frac{a_w^2y_0^2}{2}+i\frac{a_w^2}{2}\frac{\Omega_0^2}{\Omega_w}t}},\end{aligned} \tag{C.6}$$

$$\begin{aligned}\zeta &= -\frac{y^2}{y_0^2a_w^2}\left(\lambda^2+\frac{a_w^2y_0^2}{2}+i\frac{a_w^2}{2}\frac{\Omega_0^2}{\Omega_w}t\right)+\frac{y}{y_0a_w^2}\left(2\lambda^2q_0+yy_0+ix\right)-\lambda^2q_0^2-\frac{y^2}{2a_w^2}-i\frac{E_m}{\hbar}t \\ &= \left(\frac{2yq_0}{y_0a_w^2}-\frac{y^2}{y_0^2a_w^2}-q_0^2\right)\lambda^2+i\left(\frac{y}{y_0a_w^2}x-\frac{y^2}{2y_0^2a_w^2}\frac{\Omega_0^2}{\Omega_w}t-\frac{E_m}{\hbar}t\right)\end{aligned} \tag{C.7}$$

and

$$\alpha = \frac{1}{\sqrt{\frac{\lambda^2}{y_0^2}+\frac{a_w^2}{2}+i\frac{a_w^2}{2y_0^2}\frac{\Omega_0^2}{\Omega_w}t}}. \tag{C.8}$$

Our integral can then be solved as [28]

$$\begin{aligned}\Psi_0(x,y,t) &= A\int_{-\infty}^{\infty}dke^{-k^2+\xi k+\zeta}H_m(\alpha k) = Ae^{\frac{\xi^2}{4}+\zeta}\int_{-\infty}^{\infty}dke^{-(k-\frac{\xi}{2})^2}H_m(\alpha k) \\ &= Ae^{\frac{\xi^2}{4}+\zeta}\sqrt{\pi}(1-\alpha^2)^{\frac{m}{2}}H_m\left(\frac{\alpha\xi}{2(1-\alpha^2)^{\frac{1}{2}}}\right) \\ &= -\sqrt{\frac{\pi}{2^m\pi^{\frac{1}{2}}m!a_w\left(\lambda^2+\frac{a_w^2y_0^2}{2}+i\frac{a_w^2}{2}\frac{\Omega_0^2}{\Omega_w}t\right)}}\exp\left\{\frac{\left[\left(\frac{2y}{y_0a_w^2}-2q_0\right)\lambda^2+i\left(\frac{y}{y_0}\frac{\Omega_0^2}{\Omega_w}t-x\right)\right]^2}{4\left(\lambda^2+\frac{y_0^2}{2a_w^2}+i\frac{a_w^2}{2}\frac{\Omega_0^2}{\Omega_w}t\right)}\right. \\ &+ \left.\left(\frac{2yq_0}{y_0a_w^2}-\frac{y^2}{y_0^2a_w^4}-q_0^2\right)\lambda^2+i\left(\frac{y}{y_0a_w^2}x-\frac{y^2}{2y_0^2a_w^2}\frac{\Omega_0^2}{\Omega_w}t-\frac{E_m}{\hbar\Omega_w}t\right)\right\} \\ &\times \left[\frac{\lambda^2-\frac{y_0^2a_w^2}{2}+i\frac{a_w^2}{2}\frac{\Omega_0^2}{\Omega_w}t}{\lambda^2+\frac{y_0^2a_w^2}{2}+i\frac{a_w^2}{2}\frac{\Omega_0^2}{\Omega_w}t}\right]^{\frac{m}{2}}H_m\left(\frac{y_0a_w^2}{2}\frac{\left(\frac{2y}{y_0a_w^2}-2q_0\right)\lambda^2+i\left(\frac{y}{y_0}\frac{\Omega_0^2}{\Omega_w}t-x\right)}{\sqrt{\left(\lambda^2+i\frac{a_w^2}{2}\frac{\Omega_0^2}{\Omega_w}t\right)^2-\frac{y_0^4a_w^4}{4}}}\right)\end{aligned} \tag{C.9}$$

The result in equation C.9 is then used in the numerical calculations. But if we look at this result furter we see that the probability distribution for the packet is

$$
\begin{aligned}
|\Psi_0(x,y,t)|^2 &= \frac{\pi}{2^m \pi^{\frac{1}{2}} m! a_w \sqrt{\left(\lambda^2 + \frac{a_w^2 y_0^2}{2}\right)^2 + \frac{a_w^4 \Omega_0^4}{4\Omega_w^2} t^2}} \\
&\times \exp\left\{ - \frac{\lambda^2 a_w^2 \frac{\Omega_0^2}{\Omega_w} t \left[\frac{2y}{y_0 a_w^2} - 2q_0\right] \left[\frac{y\Omega_0^2}{y_0 \Omega_w} t - x\right] - \lambda^4 \left[\frac{2y}{y_0 a_w^2} - 2q_0\right]^2 \left[\lambda^2 + \frac{y_0^2}{2a_w^2}\right]}{2\left[\left(\lambda^2 + \frac{y_0^2}{2a_w^2}\right)^2 + \frac{a_w^4 \Omega_0^4}{4\Omega_w^2} t^2\right]} \right. \\
&- \left. \frac{\left[\frac{y\Omega_0^2}{y_0 \Omega_w} t - x\right]^2 \left[\lambda^2 + \frac{y_0^2}{2a_w^2}\right]}{2\left[\left(\lambda^2 + \frac{y_0^2}{2a_w^2}\right)^2 + \frac{a_w^4 \Omega_0^4}{4\Omega_w^2} t^2\right]} + 2\lambda^2 \left[\frac{2yq_0}{y_0} - \frac{y^2}{y_0^2} - q_0^2\right] \right\} \\
&\times \left(\frac{\left(\lambda^2 - \frac{y_0^2}{2a_w^2}\right)^2 + \frac{a_w^4 \Omega_0^4}{4\Omega_w^2} t^2}{\left(\lambda^2 + \frac{y_0^2}{2a_w^2}\right)^2 + \frac{a_w^4 \Omega_0^4}{4\Omega_w^2} t^2} \right)^{\frac{m}{2}} \left| H_m \left(\frac{y_0}{2a_w} \frac{\left(\frac{2y}{y_0 a_w^2} - 2q_0\right) \lambda^2 + i \left(\frac{y}{y_0} \frac{\Omega_0^2}{\Omega_w} t - x\right)}{\sqrt{\left(\lambda^2 + i \frac{a_w^2}{2} \frac{\Omega_0^2}{\Omega_w} t\right)^2 - \frac{y_0^4 a_w^4}{4}}} \right) \right|^2 .
\end{aligned}
\tag{C.10}
$$

If we compare equation (C.10) to the one dimensional case [27], where[1]

$$
|\psi(x,t)|^2 = \sqrt{\frac{2}{\pi a^2}} \frac{1}{\sqrt{1 + \frac{4\hbar^2 t^2}{m^2 a^4}}} \exp\left\{ - \frac{2a^2 \left(x - \frac{\hbar k_0}{m} t\right)^2}{a^4 + \frac{4\hbar^2 t^2}{m^2}} \right\} \tag{C.11}
$$

gives the width

$$
\Delta x(t) = \frac{a}{2} \sqrt{1 + \frac{4\hbar^2 t^2}{m^2 a^4}}, \tag{C.12}
$$

we can estimate how the width of the wavepacket in equation (C.10) should develop in time

$$
\Delta x(t) \approx \sqrt{\frac{\lambda}{2}} \sqrt{1 + \frac{a_w^4 \Omega_0^4}{4\Omega_w^2 \left(\lambda^2 + \frac{y_0^2 a_w^2}{2}\right)^2} t^2}. \tag{C.13}
$$

This can be used to configure the velocity of the wavepacket and the time length of the simulations.

[1] Here $a/2$ is the initial width of the wavepacket, k_0 the center of its momentum distribution and m the mass of the particle it represents.

Bibliography

[1] S. A. Gurvitz, Phys. Rev. B **51**, 7123 (1995).

[2] J. H. Bardarson, Master's thesis, University of Iceland, http://www.raunvis.hi.is/reports/2004/RH-09-2004.html, 2004.

[3] J. H. Bardarson *et al.*, Phys. Rev. B **70**, 245308 (2004).

[4] V. Gudmundsson *et al.*, Phys. Rev. B **71**, 235302 (2005).

[5] G. Cattapan and E. Maglione, Am. J. Phys. **71**, 903 (2003).

[6] O. Entin-Wohlman, A. Aharony, and Y. Levinson, Phys. Rev. B **65**, 195411 (2002).

[7] B. Szafran and F. M. Peeters, Phys. Rev. B **72**, 165301 (2005).

[8] S. Kurth *et al.*, Phys. Rev. B **72**, 035308 (2005).

[9] V. Moldoveanu, V. Gudmundsson, and A. Manolescu, arXiv:cond-mat/0703179v1 (2007).

[10] H. Bruus and K. Flensberg, *Many-Body Quantum Theory in Condensed Matter Physics, An Introduction* (Oxford University Press, Oxford, 2004).

[11] G. Vasile, Master's thesis, University of Iceland, http://www.raunvis.hi.is/reports/2002/RH-18-2002.html, 2002.

[12] D. F. Holcomb, Am. J. Phys. **67**, 278 (1998).

[13] D. Chouvaev, L. Kuzmin, D. S. Golubev, and A. D. Zaikin, Phys. Rev. B **59**, 10599 (1999).

[14] S. Datta, *Electronic Transport in Mesoscopic Systems* (Cambridge University Press, Cambridge, 1995).

[15] B. Hackens *et al.*, Nature Physics **2**, 826 (2006).

[16] K. E. Aidala, R. E. Parrott, E. J. Heller, and R. M. Westervelt, arXiv:cond-mat/0603035v1 (2006).

[17] P. F. Fontein, P. Hendriks, and J. H. Wolter, Surface Science **229**, 47 (1990).

[18] B. A. Lippmann and J. Schwinger, Phys. Rev. **79**, 469 (1950).

[19] C. Cohen-Tannoudji, B. Diu, and F. Laloë, *Quantum Mechanics* (John Wiley & Sons, Inc., New York, 1977), Vol. 2.

[20] M. Prusty and H. Schanz, Phys. Rev. Lett. **98**, 176804 (2007).

[21] V. Gudmundsson *et al.*, The European Physical Journal B - Condensed Matter and Complex Systems **45**, 339 (2005).

[22] V. Gudmundsson, C.-S. Tang, and A. Manolescu, Phys. Rev. B **72**, 153306 (2005).

[23] R. B. Laughlin, Phys. Rev. B **27**, 3383 (1983).

[24] R. H. Landau, *Quantum Mechanics II, A Second Course in Quantum Theory* (John Wiley & Sons inc., New York, 1996).

[25] S. Hassani, *Mathematical Physics, A Modern Introduction to Its Foundations* (Springer-Verlag New York Inc., New York, 1999).

[26] C. F. Gerald and P. O. Wheatley, *Applied Numerical Analysis*, 7th ed. (Pearsone Education Inc., Boston, 2004).

[27] C. Cohen-Tannoudji, B. Diu, and F. Laloë, *Quantum Mechanics* (John Wiley & Sons, Inc., New York, 1977), Vol. 1.

[28] I. S. Gradshteyn and I. M. Ryzhik, *Table of Integrals, Series and Products*, 6th ed. (Academic Press Inc., San Diego, 2000).